Geophysical Journal International

Geophys. J. Int. (2016) **207,** 457–480
Advance Access publication 2016 July 30
GJI Geodynamics and tectonics

doi: 10.1093/gji/ggw280

Recent kinematics of the tectonic plates surrounding the Red Sea and Gulf of Aden

Antonio Schettino,[1] Chiara Macchiavelli,[1,2] Pietro Paolo Pierantoni,[1] Davide Zanoni[3] and Najeeb Rasul[4]

[1]*School of Science and Technology – Geology Division, University of Camerino, Via Gentile III da Varano, I-62032 Camerino (MC), Italy. E-mail: antonio.schettino@unicam.it*
[2]*Institute of Earth Sciences Jaume Almera, ICTJA-CSIC, Lluis Sole i Sabaris s/n, E-08028 Barcelona, Spain*
[3]*Dipartimento di Scienze della Terra "A. Desio", Università degli Studi di Milano, Via Mangiagalli 34, I-20133 Milano, Italy*
[4]*Saudi Geological Survey, 21514 Jeddah, Saudi Arabia*

Accepted 2016 July 25. Received 2016 July 22; in original form 2015 October 28

SUMMARY

The Red Sea and Gulf of Aden represent two young basins that formed between Africa and Arabia since the early Oligocene, floored by oceanic crust or by transitional and thinned continental crust. While in the easternmost Gulf of Aden, the rift–drift transition can be dated chron C6 (∼20.1 Ma), here we show that in the Red Sea the first pulse of seafloor spreading occurred during chron C3n.2n (∼4.6 Ma) around ∼17.1°N (present-day coordinates) and propagated southwards from this location, separating the Danakil microplate from Arabia. It is also shown that seafloor spreading between Arabia and Nubia started later, around chron 2A (∼2.58 Ma), and propagated northwards. At present, there is no magnetic evidence for the existence of a linear spreading centre in the northern Red Sea at latitudes higher than ∼24°N and in the southern Red Sea below ∼14.8°N. The present-day plate kinematics of this region can be described with high accuracy by a network of five interacting plates (Nubia, Arabia, Somalia, Sinai and Danakil) and six triple junctions. For times older than anomaly 2A (∼2.58 Ma) and up to anomaly 3, the absence of marine magnetic anomalies between Arabia and Nubia prevents a rigorous kinematic description of the five-plates system. However, there is strong evidence that the unique changes in plate motions during the last 5 Myr were a dramatic slowdown at chron C2 (∼1.77 Ma) in the spreading or extension rates along the ridge and rift axes, thereby a good representation of the real plate motions can be obtained anyway by backward extension of the oldest Arabia–Nubia and Arabia–Danakil stage rotations determined on the basis of marine magnetic anomalies, respectively, C2–C2A and C2A–C3. The proposed kinematic reconstructions are accompanied by a geodynamic explanation for the genesis of large continent–continent fracture zones at the rift–drift transition and by an analysis of the strain associated with plate motions in Afar, northeastern Egypt and Sinai.

Key words: Magnetic anomalies: modelling and interpretation; Marine magnetics and palaeomagnetics; Neotectonics; Kinematics of crustal and mantle deformation.

1 INTRODUCTION

Understanding the kinematics of the tectonic plates surrounding the Red Sea–Gulf of Aden represents a fundamental step towards a comprehension of the geodynamic processes that lead to the split of a continental plate and to the development of a new ocean. While the rifting and spreading history of the Gulf of Aden is well constrained by marine magnetic anomalies, fracture zones and seismic profiles, which have allowed accurate descriptions until recent times (e.g. d'Acremont *et al.* 2005; Fournier *et al.* 2010; Leroy *et al.* 2010), plate motions around the Red Sea and along the East African Rift (EAR) are less constrained by existing geophysical data, thereby the kinematic circuits in a large area between the eastern Mediterranean and the Indian ocean have not yet received a satisfactory description.

The main source of the difficulties that are encountered in the study of the Red Sea tectonics is associated with the young age of its oceanic crust, the scarcity of large-offset transform faults and the apparent lack of fracture zones. So far, these features have represented a major obstacle preventing a reliable determination of relative motion directions between Arabia and Nubia (Chu & Gordon 1998). Chu & Gordon (1998) stressed the fact, known since the 1970s, that the strike of small-offset transform faults does not necessarily coincide with the real spreading direction. Therefore, they fundamentally used only marine magnetic

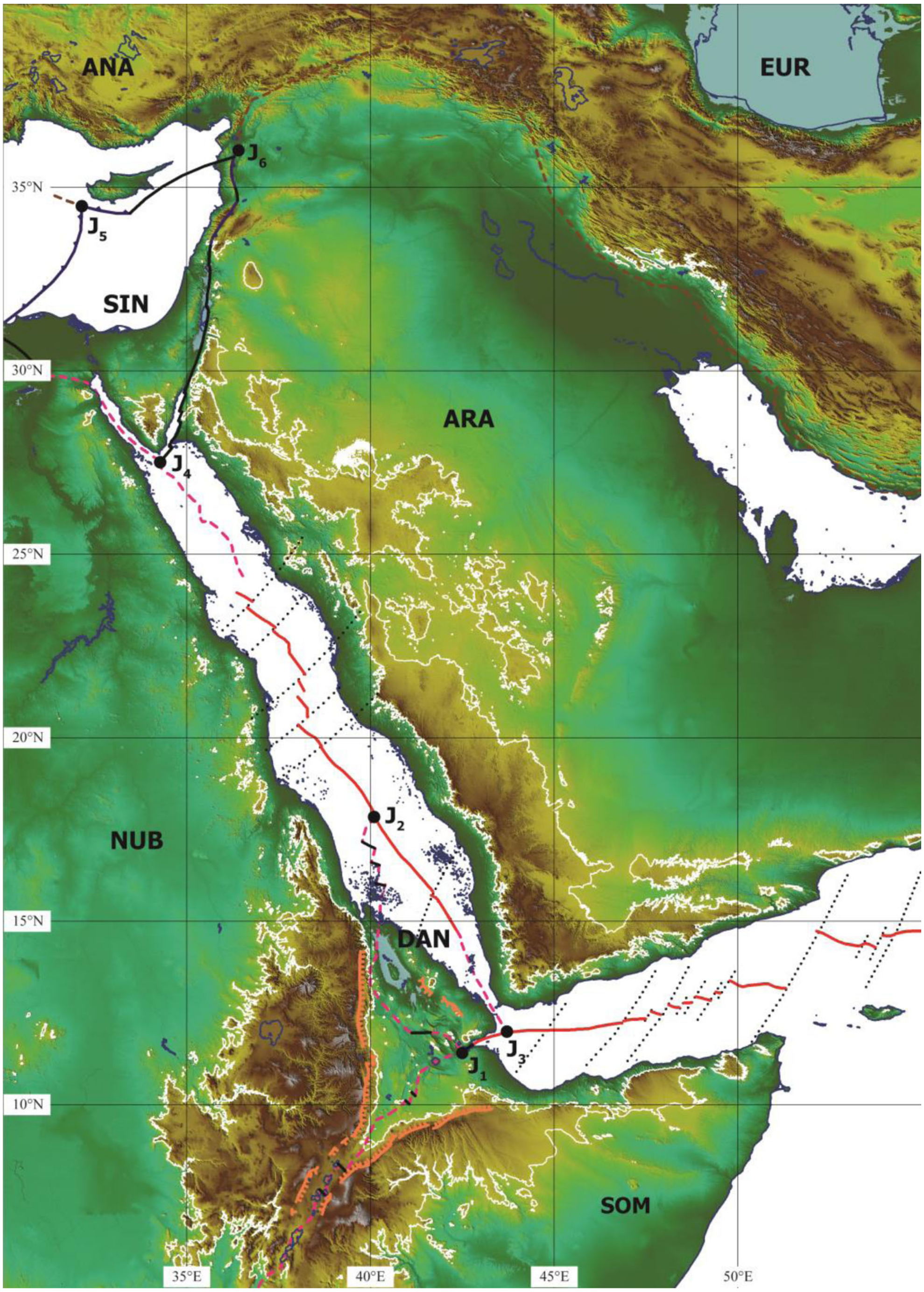

Figure 1. Location map of the study area, showing present-day plate boundaries, triple junctions and transverse structures around the Red Sea and Gulf of Aden. Red solid lines: mid-ocean ridges; red dashed lines: rift axes; black dotted lines: fracture zones and transverse structures; black solid lines: strike–slip faults; blue lines with barbs: convergent boundaries; black dashed lines: plate boundaries outside the study area; white line: 1000 m topography contour; orange lines with barbs: main rift shoulders; black dots: triple junctions; ANA = Anatolia, EUR = Eurasia, SIN = Sinai, ARA = Arabia, NUB = Nubia, DAN = Danakil, SOM = Somalia. Areas in blue are continental inland below sea level. Fracture zones in the Gulf of Aden are from Leroy *et al*. (2012).

anomalies to constrain the plate kinematics around the Red Sea. More recent studies have determined the current motion of the Arabian plate on the basis of geodetic (GPS) data (ArRajehi *et al*. 2010; McClusky *et al*. 2010).

Another problem in reconstructing plate motions around the Red Sea–Gulf of Aden region arises from the presence of two intervening microplates between Africa and Arabia. They are the Sinai and Danakil blocks (Fig. 1), whose Euler poles of relative motion with respect to Nubia have changed continuously during the last millions of years. Evidence for the existence of an independent Danakil microplate in the Afar region was presented since the late 1970s (e.g. Le Pichon & Francheteau 1978; Courtillot *et al*. 1984). With the exception of the work of Chu & Gordon (1998), existing kinematic models describing the tectonic evolution of this block are ultimately based on structural (e.g. Collet *et al*. 2000; Eagles *et al*. 2002), geodetic (e.g. McClusky *et al*. 2010), or palaeomagnetic (e.g. Manighetti *et al*. 2001) observations from Afar and the southern Red Sea. Although in principle kinematic models based on these kind of data could be affected by local rotations associated with strain partitioning, all these studies exhibit a substantial agreement with the regional model of Chu & Gordon (1998), which predicts that Danakil rifted away from the African margin through a large rotation about an Euler pole located in Eritrea, not far from the northern tip of this block. Such a widely accepted class of crank-arm models (Sichler 1980; Souriot & Brun 1992) is appealing, especially because it accounts for the triangular morphology of the Afar depression. Therefore, so far it has been questioned only by a few authors, notably by Eagles *et al*. (2002) and Wolfenden *et al*. (2004).

Clearly, the crank-arm paradigm must be considered at best as a useful approximation, because the laws of plate kinematics exclude that a fixed pole of rotation can describe the relative motion of Danakil with respect to Nubia. Granted that Nubia–Arabia and Danakil–Arabia are conjugate plates pairs, so that they move about Euler poles that are fixed in the Arabian plate reference frame during each tectonic stage, than the motion of Danakil with respect to Nubia must be characterized by a continuously changing Euler pole. Here, we shall prove that in the reference frame of Nubia this pole migrated by ∼390 km during the last 4.6 Myr, starting from a location in the central Red Sea.

Regarding the Sinai block (Fig. 1), several authors have assumed that it is now part of the African plate (Joffe & Garfunkel 1987; Le Pichon & Gaulier 1988; Jestin *et al*. 1994), thereby strike–slip motion along the Dead Sea Fault Zone (DSFZ) can be used to constrain the relative positions of Arabia with respect to Africa during the last 10–13 Myr. However, both GPS data and the significant present-day seismicity in the Gulf of Suez, in Egypt, and in the eastern Mediterranean point to the existence of an independent Sinai microplate (Badawy & Horváth 1999; Salamon *et al*. 2003; Badawy 2005; Mahmoud *et al*. 2005; Hussein *et al*. 2006; Dahy 2010; Hosny *et al*. 2013). Therefore, directional data from the DSFZ can only be used to constrain the relative motion of Sinai with respect to Arabia. We shall prove that the Euler pole proposed by Jestin *et al*. (1994) for the rotation of Arabia with respect to Africa substantially coincides with a pole describing the relative motion of Arabia with respect to the Sinai block. We shall also prove that, in a similar way to Danakil, the relative motion of Sinai with respect to Nubia is described by a continuously changing Euler pole that migrated by ∼200 km during the last 1.77 Myr.

In this paper, we show that the existing potential field and seismic data can be combined with geological observations obtained during two field surveys performed in 2015 and 2016 along the Arabian margin to constrain the plate kinematics around the Red Sea since the early Pliocene. Therefore, differently from Chu & Gordon (1998), we will combine an analysis of marine magnetic data from the Red Sea with directional data (either transform fault and fracture zone azimuths, or pattern of strike–slip faults associated with lateral shearing) to build a kinematic model for the last 4.6 Myr. We are going to present evidence that some oceanic transforms are aligned of with major transcurrent faults within the continental margins, as a result of the process of progressive oceanization of a rift basin. The diachronous formation of new spreading segments determines the reactivation and inversion of strike–slip faults at the onset of seafloor spreading. These strike–slip faults then evolve into transform faults offsetting spreading ridge segments and large primary continent–continent fracture zones. In the case of the Red Sea, there is no evidence that the Euler poles of relative motion have changed during the last 27 Myr. Therefore, both the alignment of transform faults with continental strike–slip faults and the azimuth of syn-rift strike–slip faults can be used to constrain these Euler poles.

Our starting point will be an analysis of magnetic and gravity anomalies, with the objective to produce an isochron map for the Red Sea. Then, we will use this result in conjunction with recent rotation parameters for the Gulf of Aden to build a comprehensive kinematic model predicting current plate velocities across the EAR, the Gulf of Suez, the eastern Mediterranean and Afar. This model will be representative of plate motions in a region extending from the eastern Mediterranean to central Africa during the last 1.77 Myr. Finally, taking into account that the stage poles locations of Nubia and Danakil with respect to Arabia seem to be stationary during the last 5 Myr, we show that a robust kinematic model can be created, which describes accurately the scenario in which the first oceanic crust formed in the Red Sea at ∼4.62 Ma.

2 FORMATION OF TRANSVERSE STRUCTURES IN THE RED SEA

In addition to magnetic anomaly crossings, a quantitative determination of the seafloor spreading history of an oceanic basin requires the identification of transform faults and fracture zone trends. Chu & Gordon (1998) argued that transform fault offsets in the Red Sea are useless because they never exceed 5 km, but this is undoubtedly true only in the case of the southern region, where the oldest magnetic lineations are not associated with significant transform faults. Conversely, magnetic and gravity data show that six transform faults with offsets ranging between 10 and 35 km can be observed in the northern and central Red Sea (Fig. 1), and a prolongation of these lineaments towards and across the thinned continental margins is evident on geological and high-resolution topographic maps as well as through the analysis of potential field data.

Izzeldin (1989) first suggested the possibility to identify a consistent set of large transverse structures in the pattern of gravity and magnetic anomalies, which are representative of the directions of relative motion in the Red Sea. In order to clarify the origin of these structures, which must not be confused with the usual fracture zones, we need to give a close look at the process of oceanization of a rift basin. Geological and geophysical evidences show that oceanization does not occur by continuous, regular changes, but it proceeds by steps, with the development of new linear spreading segments by coalescence of small oceanic cells that form within the areas of maximum extension (Bonatti 1985). The sketch map in Fig. 2 illustrates the process of formation of a mid-ocean ridge by successive additions of younger linear spreading segments in the direction of the Euler pole of relative motion. Geological evidence also suggests that the formation of a new segment can be accompanied by an episode of post-rift contraction and inversion of the rift structures along the continental margins (Withjack *et al*. 1995; Schlische *et al*. 2003). A simple explanation of this phenomenon is that an initial pulse of fast spreading accompanies the onset of oceanic accretion before that a steady state establishes. In recent studies (e.g. Lucazeau *et al*. 2008; Ligi *et al*. 2011, 2012; Korostelev *et al*. 2015, 2016), it has been suggested that a rapid active pulse of seafloor spreading at the rift–drift transition is a consequence of fast mantle upwelling associated with edge-driven convection. In this instance, the increased velocity of asthenosphere upwelling would be determined by the positive feedback of small-scale convective cells that form when the rising of hot-melt-rich low-viscosity mantle material produces a sharp horizontal thermal gradient with respect to the nearby cold continental lithosphere. An apparently alternative but possibly complementary mechanism could be that the initial fast asthenosphere upwelling is completely passive and driven by the extra

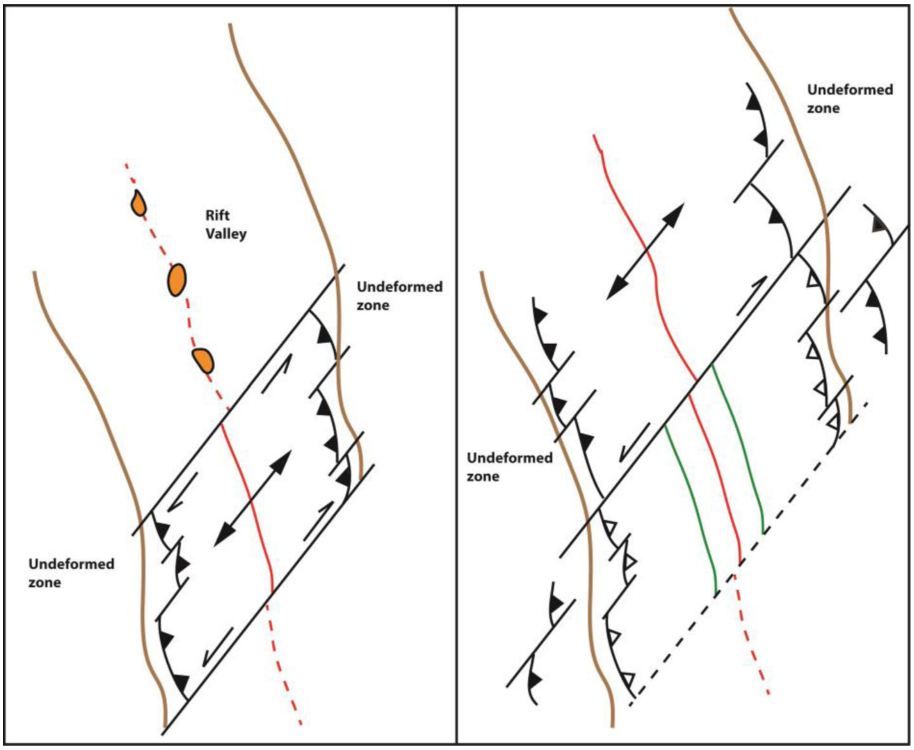

Figure 2. A model of formation of continent–continent fracture zones. Left: a linear spreading segment (red solid line) forms in the southern region of a rift basin. In a short time interval preceding steady spreading, a fast spur determines inversion of the rift structures along the continental margins (black lines with barbs) and the formation of left-lateral and right-lateral transcurrent faults at the northern boundary with the rift region (black lines). In the northern region, rifting prevails and oceanization is confined in axial cells (orange areas). Right: the coalescence of several axial cells determines the formation of a new spreading segment, with associated initial fast pulse. New compressional structures form along the margins of the northern area and the former transcurrent faults are inverted. In the southern area, anelastic relaxation of the extended margins could continue, with formation of new comprerssional structures farther from the ridge. Green lines are oceanic isochrons.

space that forms in the axial zone as a consequence of relaxation of the extended passive margins after the breakup. This hypothesis, which is illustrated in Fig. 3, implies that during the rifting process the extended continental margins accumulate some amount of elastic strain, which cannot be released seismically. After the onset of seafloor spreading, a phase of transient creep allows to release the accumulated strain energy through anelastic relaxation. Then, the extended conjugated margins are subject to post-rift contraction and eventually to tectonic inversion of the rift structures. The existence of an initial short phase of fast spreading is also supported by seismic refraction and reflection data (e.g. Talwani & Abreu 2000) and by the existence of some edge magnetic anomalies along the rifted continental margins. For example, seismic reflection data acquired by the EDGE project off the US East Coast, accompanied by wide-angle reflection and refraction data, provided clear evidence of a very thick initial oceanic crust, characterized by seaward dipping reflectors and by a prominent magnetic anomaly known as the East Coast Magnetic Anomaly (e.g. Talwani & Abreu 2000). Such structure of the ocean–continent transition zone is compatible with a fast pulse of seafloor spreading at the rift–drift transition in the central Atlantic. In general, this process implies that transverse transcurrent faults must form along the boundaries of each new oceanized sector, as illustrated in Fig. 2. Consequently, the transverse structures observed by Izzeldin (1989) should be considered as primary features that form just before the development of true transform faults and that later might evolve into continent–continent fracture zones. These transcurrent structures are associated with systems of normal faults whose trend is determined alternatively by (1) plate boundary processes and induced stress field; (2) pre-existing weakness zones or (3) lateral variations of density (Bellahsen *et al*. 2013). However, differently from the case of the Gulf of Aden (see Bellahsen *et al*. 2013), in the central and northern Red Sea the large-scale Precambrian faults exerted a strong influence on the rift geometry and controlled its evolution. Some of these faults have predominantly N–S or E–W trend, oblique with respect to both the far-field stress and the rift axis. There is strong field evidence that in the early stage of rifting these N–S and E–W structures were reactivated, respectively, as strike–slip and normal faults. In this instance, during this time interval the Arabian plate moved northwards relative to Nubia, as suggested by Makris & Rihm (1991) and by Ghebreab (1998). Other inherited structures have NW–SE trend, parallel to the main rift axis, and were reactivated later. This younger system of normal faults accommodated the extension at least since the late Oligocene (Bosworth *et al*. 2005). During this stage, the kinematics along the older system of faults changed from pure normal or pure strike–slip to dextral or sinistral transtension, respectively, in a similar way to the process described by Bellahsen *et al*. (2013) for the Gulf of Aden.

If transverse structures are effectively expression of strike–slip faulting during the oceanization process, their strike is representative of the directions of relative motion during the latest rifting stage and onset of seafloor spreading. Unfortunately, in the Red Sea region these tectonic structures are not represented by narrow seafloor features that can be easily digitized using GIS software. Consequently, many different sets of lineations that apparently fit the pattern of potential field data can be traced. It is mainly the curvature of these

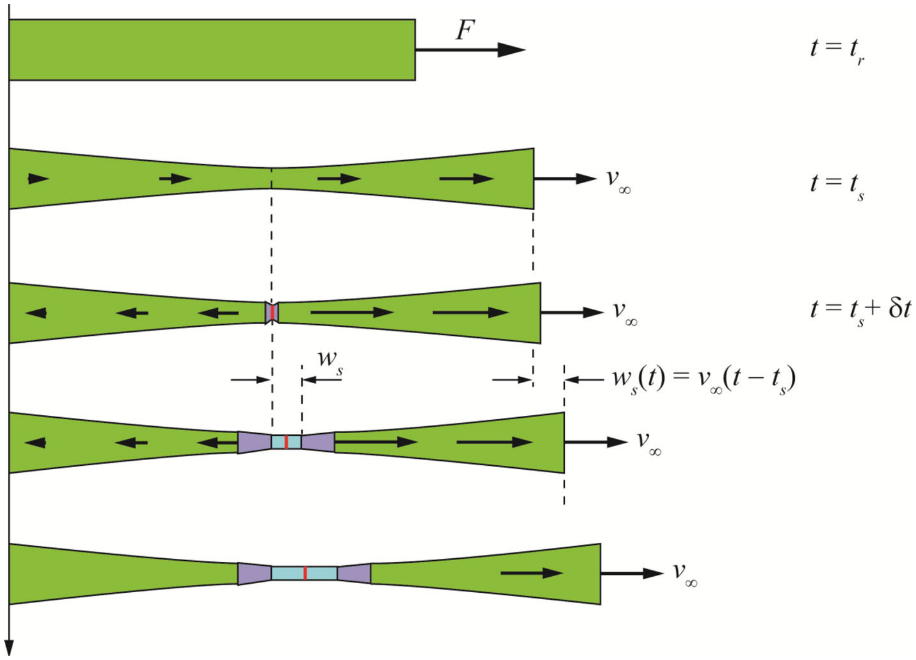

Figure 3. Sketch illustrating a possible mechanism of formation of an initial spurt of oceanic crust, associated with anelastic relaxation of the extended continental margins. At time $t = t_\mathrm{r}$ rifting starts through the application of a far-field force $\boldsymbol{F}$. It is assumed that the left border of the extending plate is kept fixed, so that all velocities are relative to this frame. The two plates move apart at constant far-field linear velocity v_∞, but the effective velocity in the deforming zone increases linearly from left to right. At time $t = t_\mathrm{s}$ rifting ends and for a short time interval δt the extended margins release the accumulated elastic strain and shrink, increasing the effective recession velocity in the axial zone. Consequently, additional oceanic crust (violet areas) is accreted to fill the extra space during the anelastic relaxation episode.

features to be unconstrained, rather than their strike. Therefore, a large uncertainty is associated with the distance of the Euler pole from the transverse structures. The only way to overcome this problem requires the use of additional constraints and data sets, such as closure of global kinematic circuits or azimuths of strike–slip faults observed on-land. For example, any solution for the Arabia–Nubia relative motion constrains the motion of Somalia with respect to Nubia and Antarctica, because the kinematics of Arabia–Somalia is assigned. It can be shown that Arabia–Nubia Euler poles too close or too far from the Red Sea region give inconsistent results along the southwest Indian Ridge (SWIR). Therefore, we tested several sets of small circle arcs, apparently compatible with the observed pattern of gravity anomalies, excluding solutions that were inconsistent with geological or kinematic constraints. We built synthetic lineaments by interactively fitting sets of small circle arcs about test Euler poles to local kinematic indicators identified in the Red Sea and along the Arabian margin. These data sets included: (1) Local azimuths of wide syn-drift transcurrent faults that represent the on land prolongation of transverse structures associated with oceanic transform faults and fracture zones; (2) azimuths of strike–slip faults associated with the syn-rift stage and (3) marine shear zones identified on the vertical derivative grid of the latest version (ver. 23) of the global free-air gravity anomaly map of Sandwell *et al.* (2014). The on-land kinematic indicators were measured during two successive geological campaigns (in 2015 and 2016) in a wide area of the Arabian margin between the provinces of Makkah and Tabuk (Pierantoni *et al.*, in preparation). All the measurements acquired along the on-land tracts of transverse structures showed evidence of recent dextral strike–slip motion, in agreement with the model illustrated in Fig. 2, and we found clear indicators of tectonic inversion at the landward termination of most structures (Fig. 5, Schettino *et al.*, preparation). Evidence of residual dextral strike–slip motion along the southernmost transverse structure, the Ad Damm fault (Fig. 4), is also provided by a set of earthquake focal mechanisms (Al-Saud 2008; Fnais *et al.* 2015). It should be noted that this structure operated as a left-lateral transfer fault during the rifting stage, as it is indicated by the orientation of sigmoidal dikes (Pallister 1986, 1987).

Other kinematic indicators were identified on the vertical derivative of the free-air gravity anomaly grid of Sandwell *et al.* (2014). Fig. 5 shows a best-fitting set of small circle arcs for the central and northern Red Sea. The Euler pole associated with these arcs resulted to be located at (30.43°N, 27.41°E), with an rms error of fit between kinematic indicators and small circle arcs of $\varepsilon = 0.0015^\circ$. For the southern Red Sea, the best-fitting small circle arcs (Fig. 6) have an Euler pole at (11.90°N, 50.22°E), with an rms error $\varepsilon = 0.0061^\circ$ with respect to the identified azimuths.

Points sampled along synthetic transverse structures that have been determined using the procedure discussed above can be used, in conjunction with magnetic anomaly crossings, to calculate an Euler pole of relative motion and associated angle of rotation. Of course, the final result will not necessarily coincide with the Euler pole determined on the basis of kinematic indicators alone, but will be close to it, granted that the number of magnetic crossings balances the fracture zone crossings sampled along the small circle arcs.

3 SEAFLOOR SPREADING IN THE RED SEA

In this study, we consider 18 marine surveys from the NGDC GEODAS database for the Red Sea region (Fig. 7), from which 103

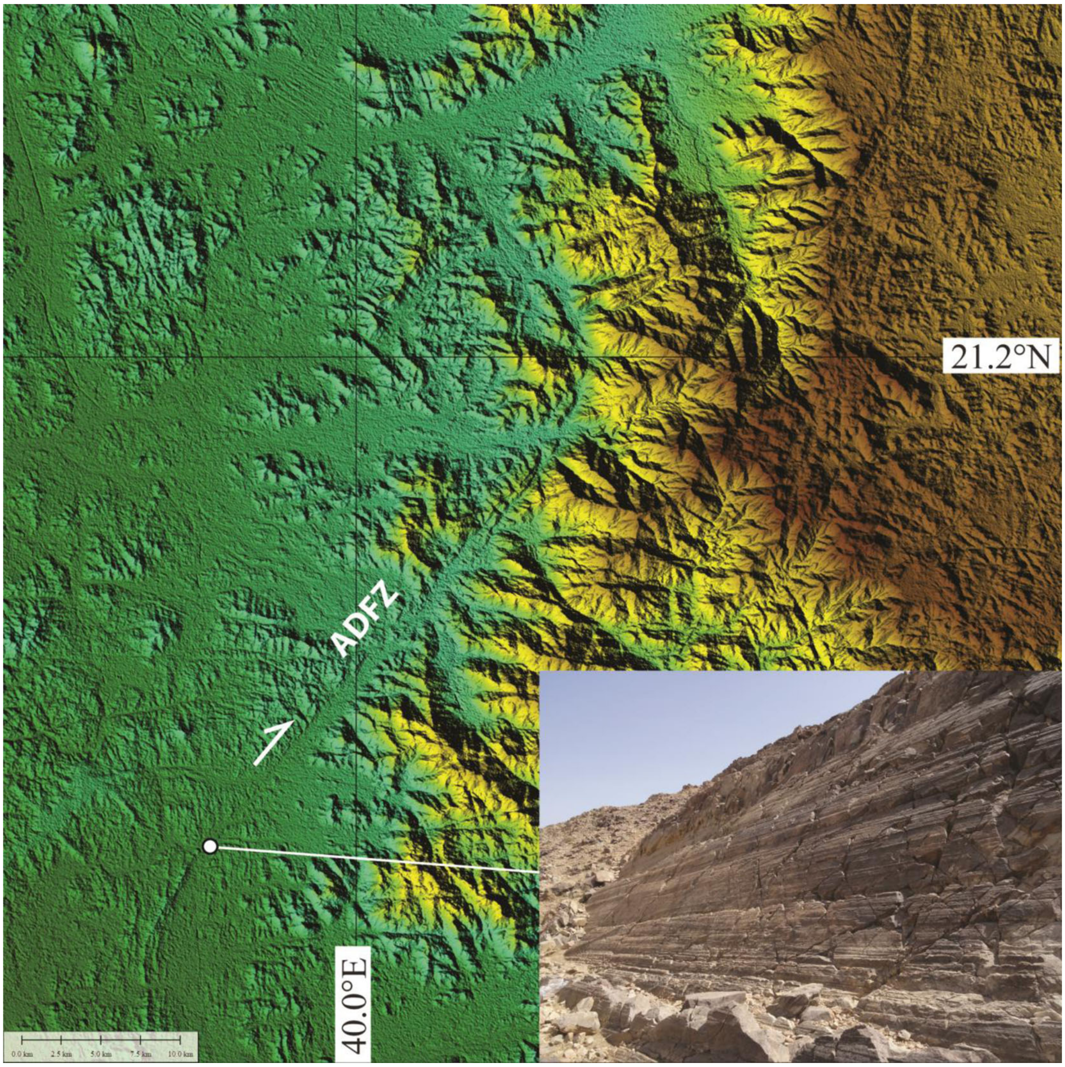

Figure 4. High-resolution ASTER–GDEM topography of the Arabian margin near Jeddah and Makkah, showing the trace of the Ad Damm fault zone (ADFZ). Inset displays a measurement station of the 2015 campaign. The location of this outcrop, which shows clear kinematic indicators of strike–slip motion, is indicated by the white circle.

magnetic profiles were extracted and analysed using an interactive software tool for the analysis of marine magnetic anomalies (Schettino 2012). They are shown in Fig. 8. Thirty four of these profiles were discarded because of their low quality, or because they were located on continental crust in the northern Red Sea. The remaining 68 profiles furnished a consistent data set of anomaly crossings, and for the large majority of them we found a good or excellent magnetization model in the forward modelling procedure (Fig. 9). Only six profiles included data collected during disturbed days, and for five of them the *Kp* index did not exceed four.

A correlation map of identified magnetic anomalies through the 68 profiles analysed in this study can be found in the Supporting Information. The corresponding crossings of anomalies 2 (1.77 Ma), 2A (2.58 Ma) and 3 (4.18 Ma) are illustrated in Figs 10(A), (B) and (C), respectively. The geomagnetic polarity timescale of Cande & Kent (1995) was used in all spreading rate determinations. The oldest oceanic crust was found along a profile crossing the spreading ridge at 17.1°N. It has an age of 4.62 Ma. Figs 10(A)–(C) show that anomalies 2 and 2A extend from ∼15.5°N in the southern Red Sea to ∼22.5°N in the northern sector, whereas anomaly 3 can be found only between 15.7°N and 18.1°N. A major problem in the identification of these anomalies was associated with the presence of thick salt and layered evaporites just above the oceanic crust, which prevented to model the magnetic basement through bathymetry. We assumed the following simple relationship between bathymetry z and depth to the basement z':

$$z' = z - \alpha x \tag{1}$$

where x is the distance from the ridge axis and α is a depth modifier selected during the forward modelling procedure to account for a realistic thermal subsidence rate. An example of relation between magnetic basement and bathymetry is illustrated in Fig. 9. The whole set of magnetic profiles showing the fit of model anomalies to the observed data can be found in the Supporting Information.

We used a version of Hellinger's algorithm (Hellinger 1981), included in the software PLACA (Matias *et al*. 2005), to determine finite reconstruction poles for anomalies 2, 2A and 3. A statistical analysis of the results showed that the set of conjugate crossings 2 and 2A north of ∼18°N was incompatible with corresponding crossings from the southern Red Sea, which is in agreement with the results of Chu & Gordon (1998). This is a consequence of the fact that the African-side oceanic crust that forms in the southern

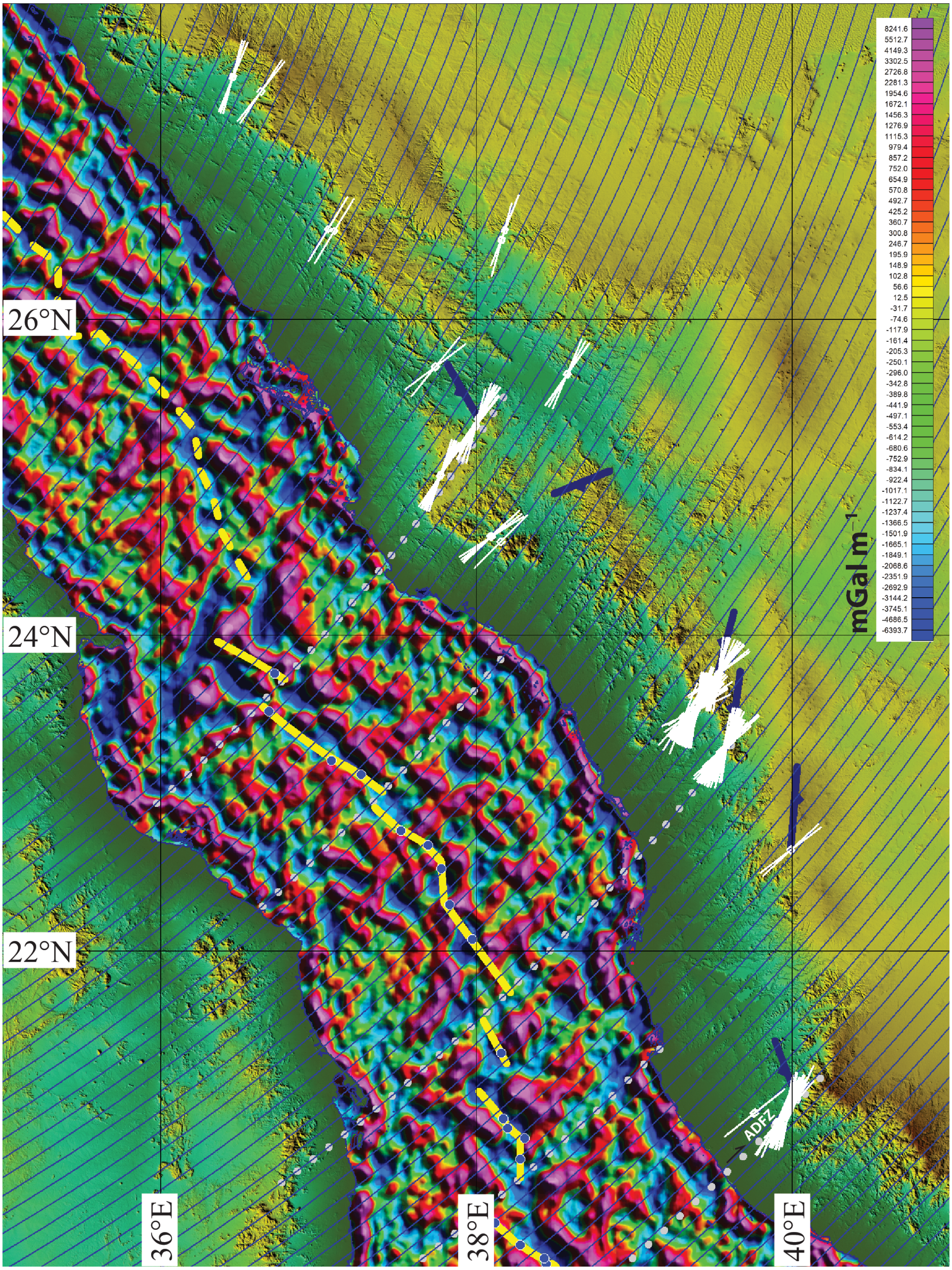

Figure 5. Best-fitting small circle arcs for the central and northern Red Sea. Ridge segmentation and major transverse structures in the central Red Sea are also shown. The background image shows the vertical derivative of free-air gravity anomalies (Sandwell *et al*. 2014). This map enhances the fine structure associated with transverse structures. Blue dots show 1n magnetic crossings that have been used to trace the ridge axis (yellow line). Dotted lines are transverse structures; White line segments are field measurements, showing the local azimuth of observed shear zones. Blue lines with triangle are observed inversion structures. The triangles are on the hangingwalls of the faults.

Red Sea belongs to the Danakil microplate, not to Nubia, and that the spreading rate decreases suddenly by ~2.5 mm yr^{-1} south of ~18°N. Therefore, an *RRR* triple junction was inserted at this latitude to separate the crossings associated with Nubia–Arabia motion from those associated with relative motion between Danakil and Arabia (Figs 10A–C). The analysis showed that not only the spreading rate is lower between the latter plate pair but also the spreading direction is different, changing from N49E just north of

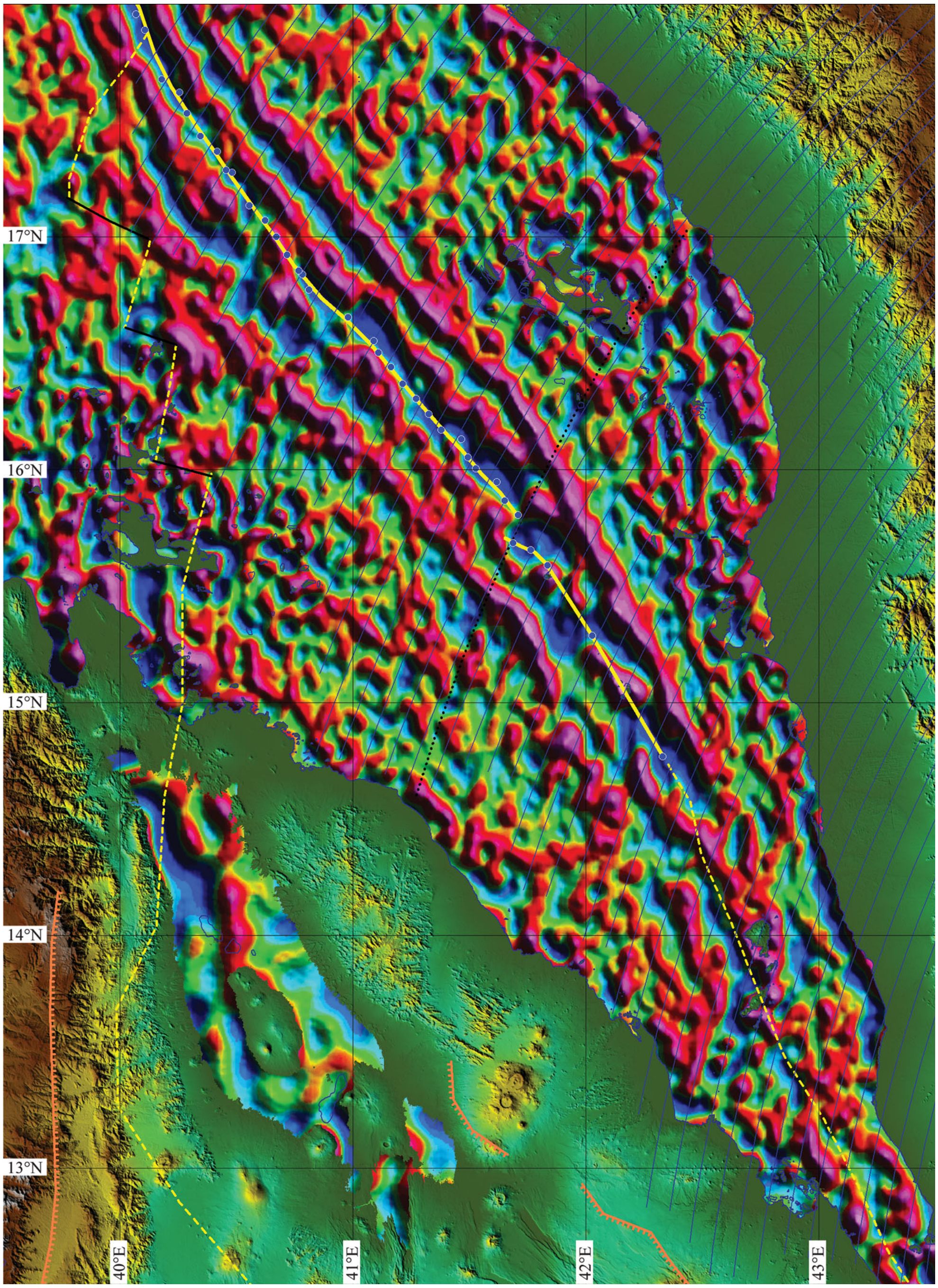

Figure 6. Best-fitting small circle arcs for the southern Red Sea. The dotted line illlustrates the estimated trend of the unique transverse structure present in the southern Red Sea.

∼18°N to N32E in the southern Red Sea. Finally and most importantly, oceanic crust having age older than chron 2A is confined to the south of the triple junction and is expression of relative motion between Danakil–Arabia before 2.58 Ma (Fig. 10C), while the northern and central Red Sea were still in a rifting phase. The final isochron map is illustrated in Fig. 10(D). It suggests that the first oceanic crust formed in the southern Red Sea in a small area around 17.1°N (present-day coordinates), presumably within a small discrete axial cell (e.g. Bonatti 1985). Isochrons 2 and 2A between Nubia and Arabia are formed, respectively, by seven and six segments, while there are three corresponding segments between Danakil and Arabia. Isochron 3 exists only between Danakil and Arabia and is formed by two segments. The total reconstruction poles associated with these isochrons, along with covariance matrices, are listed in Table 1, while confidence ellipses are illustrated in Fig. 11. These results show that the Euler pole locations for anomalies 2 and 2A are statistically undistinguishable for the Arabia–Nubia plate pair, although the angular velocities during the stages 1–2 and 2–2A are significantly different, respectively, 0.49 and 0.90°7 Myr^{-1}. Similarly, in the case of Danakil–Arabia, the reconstruction pole locations for anomalies 2, 2A and 3 are statistically undistinguishable, although the angular velocities during the stages 1–2, 2–2A and 2A–3 are somewhat different, respectively, 0.71, 0.91 and 0.86° Myr^{-1}. Therefore, it is not possible to merge these time intervals

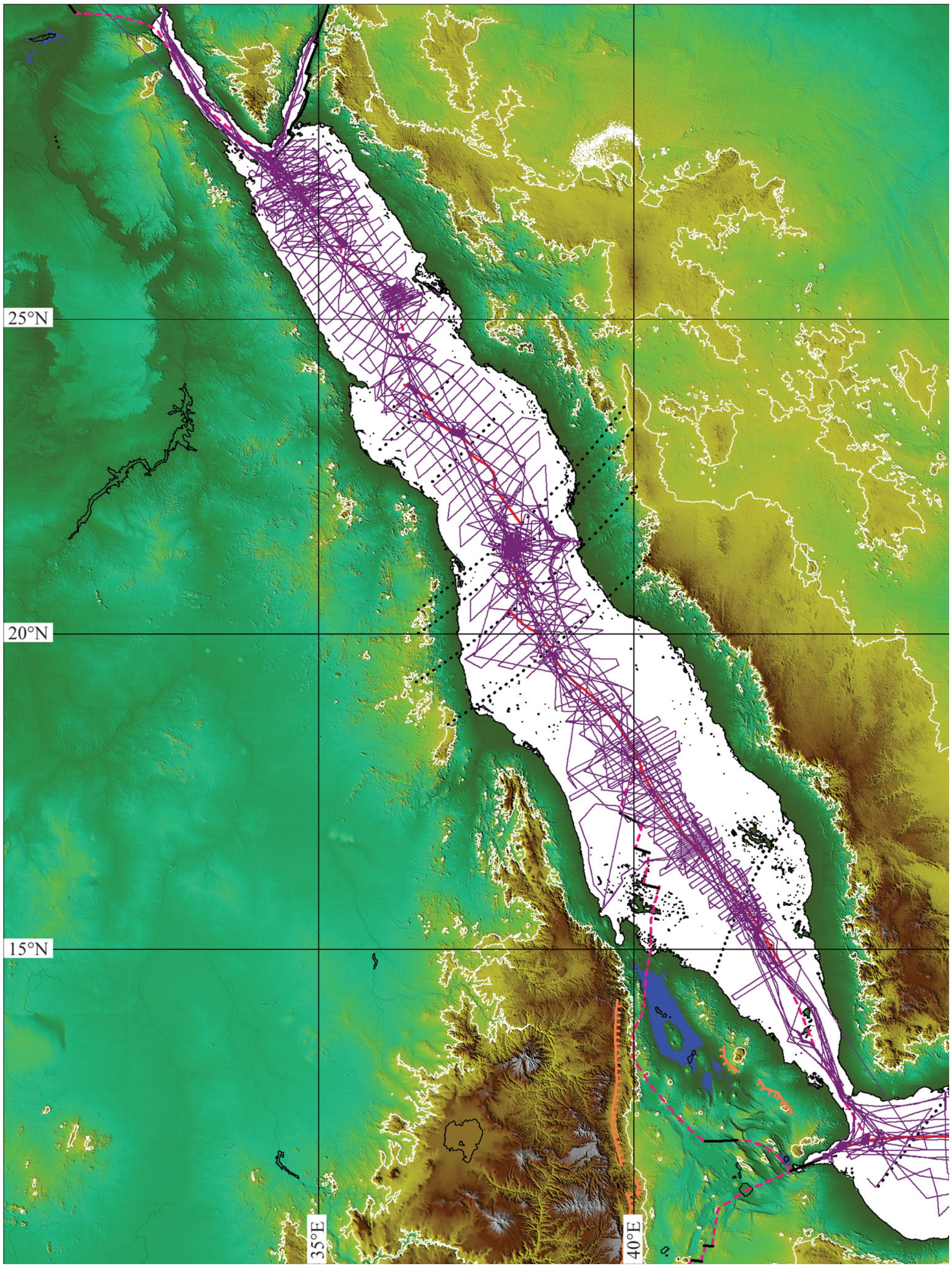

Figure 7. Ship tracks in the Red Sea from the GEODAS NGDC database.

into longer tectonic stages 1–2A or 1–3 describing single rotations of Arabia relative to Nubia or Danakil, respectively.

4 PLATE MOTIONS AROUND THE RED SEA AND GULF OF ADEN

Although formally the intervals C1–C2, C2–C2A and C2A–C3 are distinct stages, the confidence ellipses shown in Fig. 11 suggest that small differences between the reconstruction pole locations at anomalies 2, 2A and 3 (in the case of Danakil–Arabia) are not significant. Therefore, it is reasonable to assume that the Euler poles of rotation of Danakil and Nubia with respect to Arabia remained stable since the early Pliocene, irrespective of consistent changes in the angular velocities. As a consequence, in the rotation model of Table 2, which describes plate motions around the Red Sea and Gulf of Aden since the early Pliocene, we recalculated finite reconstruction angles by keeping the Euler poles of rotation fixed to the best-constrained locations, as determined by the degrees of freedom listed in Table 1. In Table 2, the oldest anomaly time for the Red Sea region is 4.62 Ma, corresponding to the top of C3n.2r. As mentioned above, this is the age of the oldest oceanic crust identified on the basis of marine magnetic anomalies. We assumed that the angular velocity of Arabia relative to Nubia during the stage 2–2A can be extrapolated backward to this time. A similar hypothesis was made in the case of the Danakil–Arabia plate pair. Both are justified by the regular trend of kinematic indicators around the Red Sea and by the observation that only in the last 2 Myr the spreading velocities have experienced a dramatic change.

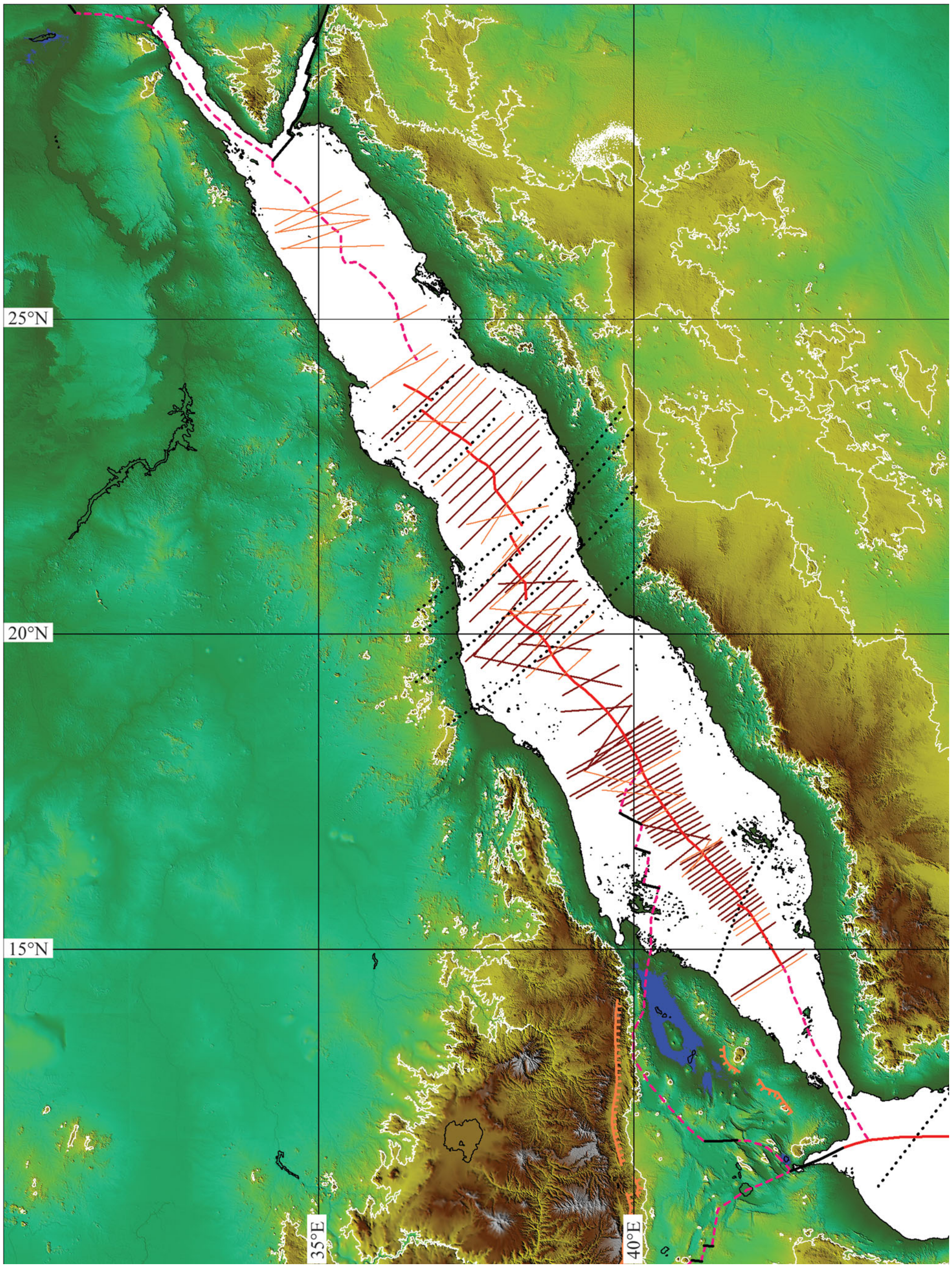

Figure 8. Traces of magnetic profiles used (brown lines) and discarded (orange lines) in this study.

An interesting implication of the rotation parameters listed in Table 2 is a dramatic slowdown at chron C2 (∼1.77 Ma) in the spreading or extension rates along the ridge and rift axes, both in the central northern (Arabia–Nubia) and in the southern Red Sea (Danakil–Arabia). Of course, in order to compare the present-day spreading velocities, predicted using classic plate kinematics methods, with GPS data or other kinematic models of current plate motions, we should correct the Euler pole relative to the youngest stage for outward displacement (DeMets & Wilson 2008). An overall estimate of this quantity can be obtained introducing the concept of angular outward displacement (Schettino & Macchiavelli 2016). However, in the case of the Red Sea it cannot be calculated, because the observed slowdown would give an inward rather than an outward displacement.

A complete kinematic model of the Red Sea–Gulf of Aden region requires specification of the motions of Somalia and Sinai relative to Arabia. The former is well constrained by marine magnetic anomalies, and in Table 2 we used a slightly modified version of the recent high-resolution model of Fournier *et al.* (2010). The latter can only be estimated on the basis of geometry and seismicity of the transcurrent boundary between Sinai and Arabia (Fig. 1). Therefore, we estimated the Euler pole associated with strike–slip motion along the DSFZ through a least-squares procedure that operated on seismic data. This procedure determined the finite reconstruction pole location that provided the best alignment of focal mechanism slip vectors with Euler pole parallels. To this purpose, we used 33 focal mechanisms from Salamon *et al.* (2003), Hofstetter *et al.* (2007) and the Centroid Moment

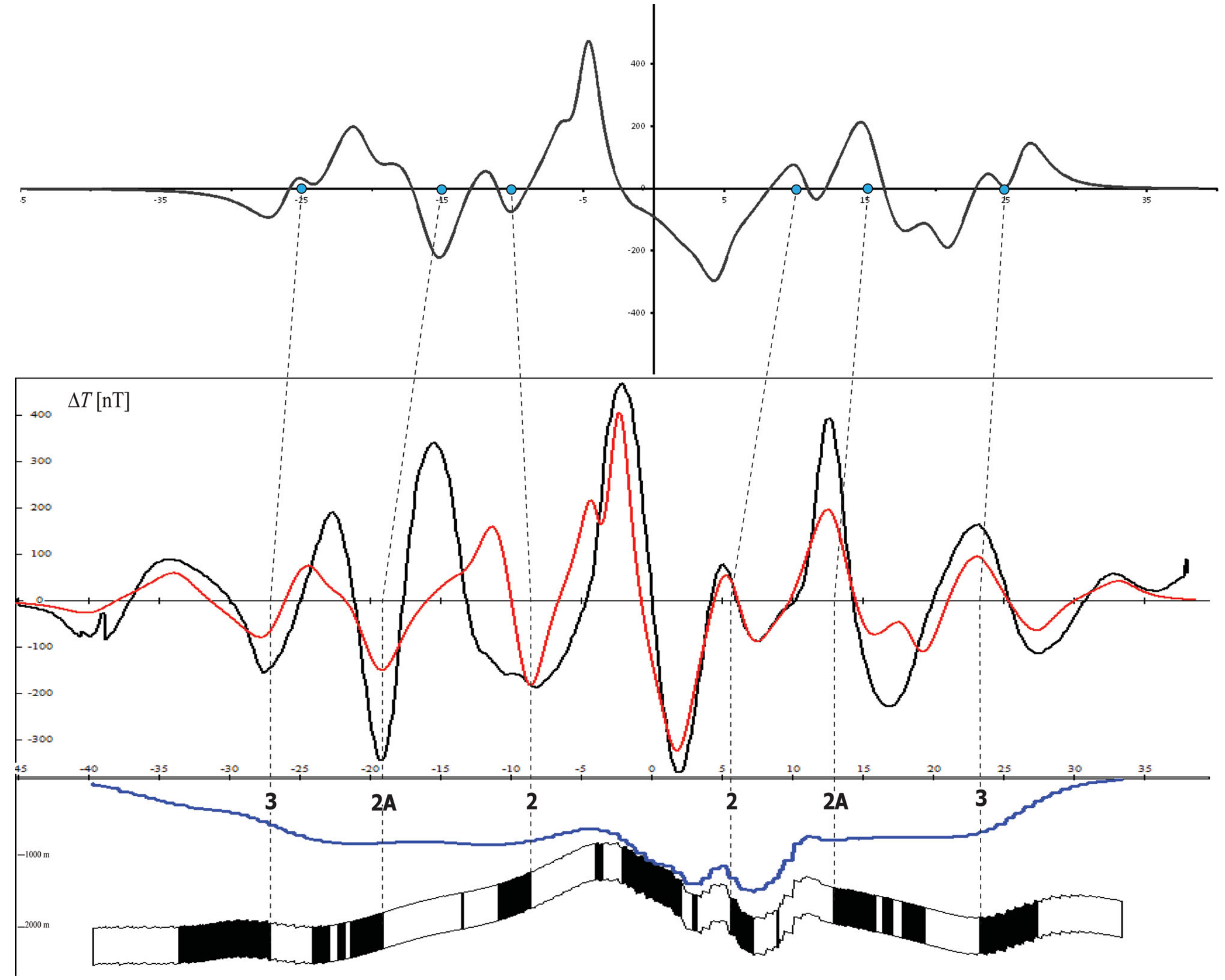

Figure 9. Correlation points of magnetic anomalies. The lower panel shows the best-fitting magnetization model and anomaly locations associated with an observed magnetic profile (middle panel: black line). The red line shows the theoretical magnetic signal generated by such magnetization distribution. The upper panel shows a constant-velocity model, obtained using the average full spreading velocity of the best-fitting model between anomaly 3 and the present.

Tensor (CMT) catalogue (Table 3 and Fig. 12). This approach furnished a pole at 32.37°N 27.02°E, with an rms error of 0.0187°. To determine the angular velocity, we first calculated the weighted average of slip rates along the DSFZ, determined by a variety of techniques and sources (Table 4), obtaining $v = 3.9 \pm 0.9$ mm yr^{-1}. Then, we calculated the angular velocity by the following formula:

$$\omega = \frac{v}{R \sin \theta_e} = 0.2764^\circ\ \mathrm{Myr}^{-1} \qquad (2)$$

where R is the Earth's radius and θ_e is the Euler pole colatitude of the DSFZ (angular distance to the Euler pole). The present-day geometry of plate boundaries in the Red Sea–Gulf of Aden region is illustrated in Fig. 1, while the detailed kinematics and predicted pattern of deformation along boundary zones is shown in Figs 13 and 14 by flow lines about Euler poles of current motion. It should be noted that in the context of the kinematic model discussed here, plate boundaries are always shown as narrow boundaries, even when they are diffuse, for example, in the eastern Mediterranean and Afar regions. The representative western and southeastern boundaries of Danakil, as well as the boundaries of the Sinai block, were traced on the basis of the highest density of seismic activity from the ISC catalogue. The tectonic style of each boundary was determined either by available double-couple focal mechanisms or from slip vectors predicted by the kinematic model of Table 2. It should be noted that the shape assumed for the Danakil microplate, in particular its southeastern boundary, is very different from that proposed by some authors (e.g. Eagles *et al*. 2002), who substantially identify the microplate with the Danakil horst. Furthermore, the abrupt southern termination of the southern Red Sea ridge at ∼14.8°N, the lack of evident extensional structures in the southernmost Red Sea towards the Bab–El–Mandeb strait, and the negligible seismicity of this area (e.g. Al-Amri *et al*. 1998) could lead to assume that a NE–SW strike–slip structure exists, which transfers extension from the Red Sea ridge to Afar. This boundary was first hypothesized by Barberi & Varet (1977) and Courtillot (1982), who called it Hanish–Dubbi transverse zone (HDTZ, Fig. 14). In this model, the southernmost Red Sea and Danakil are part of the Arabian plate, the spreading rate along the southern Red Sea ridge increases southwards, and no triple junction exists in the Bab–El–Mandeb strait. We tested extensively this kinematic scenario in a first version of this work, but the magnetic evidence shows that the spreading rate decreases from 14.2 mm yr^{-1} at ∼17.4°N to 12.0 mm yr^{-1} at ∼15.3°N, thereby the Euler pole of rotation of Danakil relative to Arabia must be located to the south. Consequently, we excluded this possibility. More to

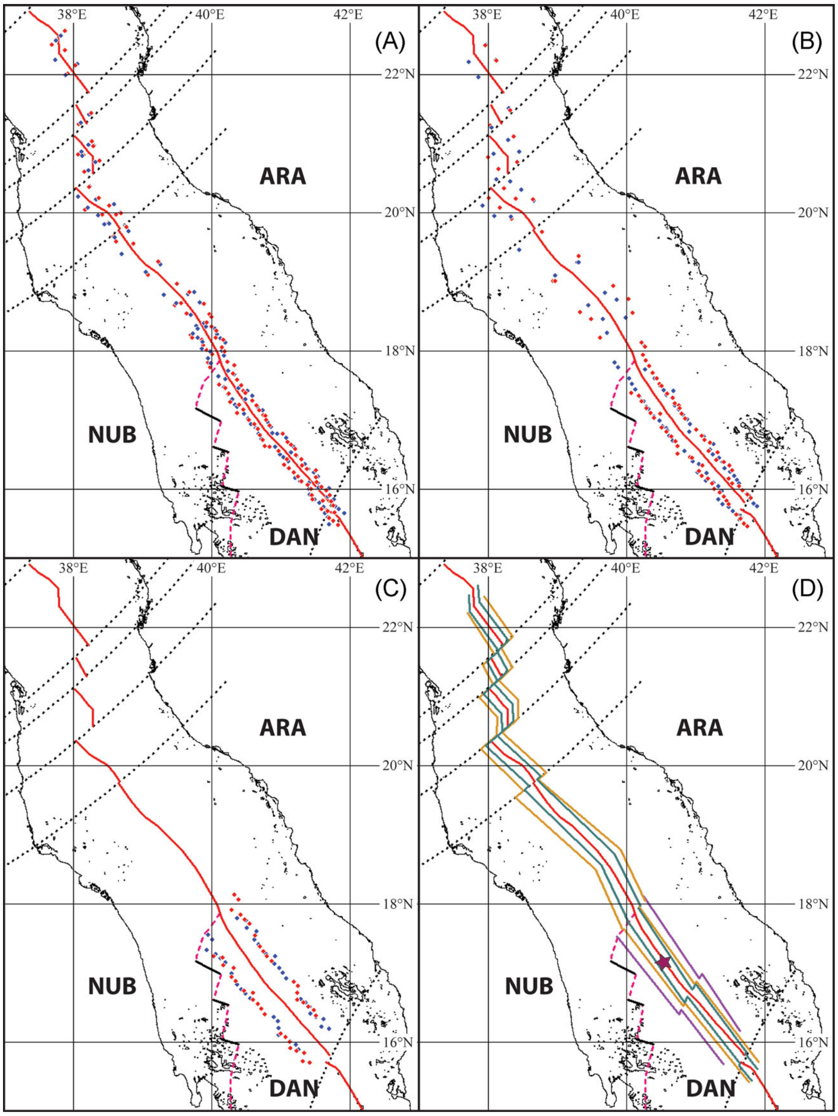

Figure 10. Panels (A), (B) and (C) show crossings of anomalies 2 (1.77 Ma), 2A (2.58 Ma) and 3 (4.18 Ma), respectively, identified in the Red Sea (blue dots) and crossings rotated according to the finite reconstruction poles of Table 1 (red dots). (D) Magnetic isochrons 2 (green), 2A (ocra) and 3 (purple). Star in the southern Red Sea indicates the location where the magnetic profile with the oldest identified oceanic crust (4.62 Ma, early Pliocene) crosses the ridge.

Table 1. Finite reconstruction poles and covariance matrices from marine magnetic anomalies.

Plate pair	*N*	Chron	Age	λ	φ	Ω	*a*	*b*	*c*	*d*	*e*	*f*
Arabia/Nubia	85	2n	1.77	30.32	27.18	–0.86	6.380	–5.056	0.436	5.031	–0.387	0.033
Arabia/Nubia	73	2An.1n	2.58	29.39	29.11	–1.80	3.442	–3.111	0.604	3.016	–0.565	0.111
Danakil/Arabia	97	2n	1.77	11.68	49.74	–1.26	2.074	–0.813	0.255	0.683	–0.143	0.038
Danakil/Arabia	95	2An.1n	2.58	11.01	51.62	–1.73	8.090	–3.960	1.234	2.142	–0.631	0.194
Danakil/Arabia	76	3n.1n	4.18	12.55	48.52	–4.05	1.329	–0.625	0.649	0.323	–0.318	0.329

Notes: N represents the degrees of freedom (total number of anomaly and fracture zone crossings minus twice the total number of anomaly and fracture zone segments minus 3.

Elements *a*, *d* and *f* are diagonal elements of the variance–covariance matrix, while *b*, *c* and *e* represent off-diagonal components.

the north, the Danakil–Nubia boundary was segmented taking into account of the presence of several CMT fault plane solutions that were previously considered as N–S sinistral strike–slip by Chu & Gordon (1998), but that we now reinterpret as E–W dextral strike–slip, according to the flow lines shown in Fig. 14. In fact, only the latter solution is compatible with the relative motion Nubia–Danakil inferred by the kinematic model of Table 2. In general, while motions of Nubia, Danakil, Sinai and Somalia with respect to Arabia are constrained by marine magnetic anomalies or seismic data, relative velocity between any other plate pair can be obtained only indirectly by combination of Euler vectors. In the case of Nubia–Danakil, the model of Table 2 predicts E to ESE displacement of Danakil relative to Nubia, thereby any strike–slip fault along the boundary must be interpreted as right lateral.

The kinematic model listed in Table 2 also allows to predict modern plate motions and pattern of deformation along the

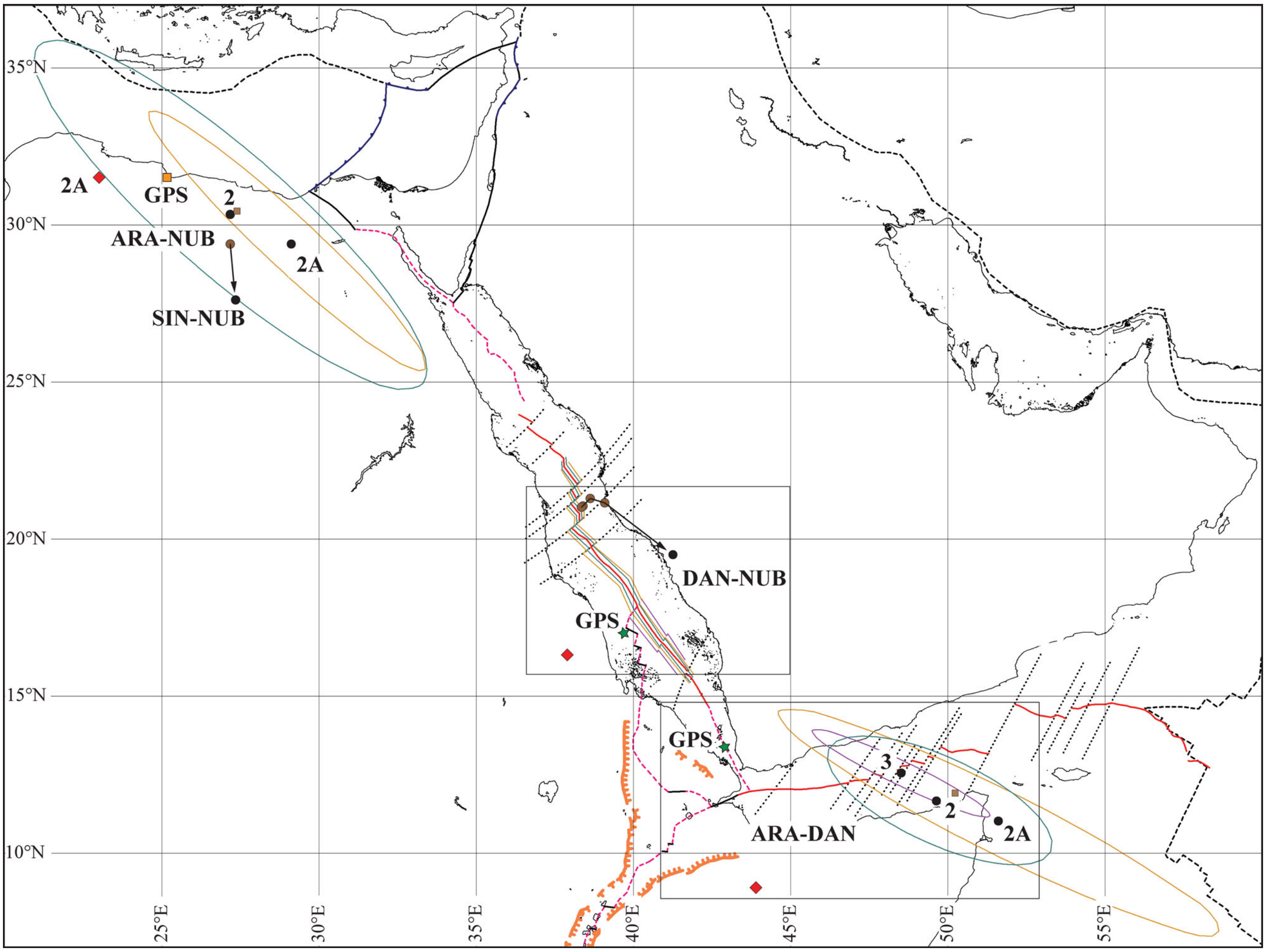

Figure 11. Euler poles (black dots) and confidence ellipses for anomalies 2 (1.77 Ma) and 2A (2.58 Ma) for Arabia–Danakil and Arabia–Nubia plate pairs and confidence ellipse for anomaly 3 (4.18 Ma) for the Arabia–Danakil plate pair. Present-day instantaneous Euler poles from some previous authors are also shown: Red rhombuses = Chu & Gordon (1998); Ocra square = Reilinger & McClusky (2011); Green stars = McClusky *et al.* (2010). Brown dots illustrate the migration of the Danakil–Nubia and Sinai–Nubia Euler poles since the early Pliocene in the reference frame of Nubia. Brown squares are Euler poles for Danakil–Arabia and Arabia–Nubia, determined by kinematic indicators only.

Table 2. Rotation model for the Red Sea and Gulf of Aden regions.

Age	Lat	Lon	Angle	References
		Arabia–Nubia		
1.77	30.32	27.18	–0.86	This paper
2.58	30.32	27.18	–1.59	This paper
4.62	30.32	27.18	–3.43	This paper
		Danakil–Arabia		
1.77	11.68	49.74	–1.26	This paper
2.58	11.68	49.74	–2.00	This paper
4.18	11.68	49.74	–3.38	This paper
4.62	11.68	49.74	–3.76	This paper
		Somalia–Arabia		
1.00	23.67	22.21	+0.52	This paper
2.58	23.67	22.21	+0.94	Fournier *et al.* (2010)
3.58	21.28	28.50	+1.62	Fournier *et al.* (2010)
5.89	25.46	25.41	+2.40	Fournier *et al.* (2010)
		Sinai–Arabia		
4.62	32.37	27.02	1.28	This paper

northern part of the EAR and in the southern Indian ocean, where the boundary between Nubia and Somalia attains the SWIR. To this purpose, we could determine the present Nubia–Somalia kinematics starting from the anomaly 2 Arabia–Nubia reconstruction and the youngest Euler pole available for Somalia–Arabia, which has age anomaly 2A (Fournier *et al.* 2010). However, it is possible to show that this procedure would lead to an incorrect description of the kinematics along the boundaries between Somalia and Nubia and between Somalia and Antarctica. Even using Chu & Gordon's (1998) Arabia–Nubia pole for the opening of the Red Sea would produce incorrect results. This longstanding problem of non-closure of the plate circuit through the Indo–Australian, Antarctic and African plates has been addressed in several papers (e.g. Chu & Gordon 1999; Horner-Johnson *et al.* 2005). Essentially, it arises from a significant difference of the Nubia–Somalia Euler vector estimated from Gulf of Aden–Red Sea data with respect to the angular velocity that can be determined using exclusively data from the SWIR. Horner-Johnson *et al.* (2005) argued that this significant difference could be indicative of the fact that Somalia is not a single rigid plate. However, the non-rigidity of the Somalian plate does not explain the discrepancy between the relative motion predicted along the EAR, which is based on marine magnetic data from the Gulf of Aden and the Red Sea, and focal mechanisms of earthquakes or GPS data from the East Africa region, because in this instance the problem is associated with the current spreading rates along the Sheba Ridge inferred from the anomaly 2A reconstruction of Fournier *et al.* (2010), which are too low. However, if we admit that

Table 3. Focal mechanisms used in the determination of the DSFZ kinematics.

Lat	Lon	Strike	Dip	Rake	Ref
27.9	34.3	220	65	−40	Salamon *et al*. (2003)
28.32	34.21	202	67	−3	Harvard CMT
28.57	34.82	205	50	−110	Salamon *et al*. (2003)
29.07	34.73	196	59	−15	Harvard CMT
30.49	35.33	207	90	12	Hofstetter *et al*. (2007)
30.53	35.18	26	74	−44	Hofstetter *et al*. (2007)
30.53	35.3	196	33	−79	Hofstetter *et al*. (2007)
30.54	35.59	197	40	−4	Harvard CMT
30.55	35.29	197	40	−75	Hofstetter *et al*. (2007)
30.55	35.25	31	69	−54	Hofstetter *et al*. (2007)
30.55	35.29	27	56	−57	Hofstetter *et al*. (2007)
30.56	35.27	194	36	−76	Hofstetter *et al*. (2007)
30.56	35.26	204	49	−72	Hofstetter *et al*. (2007)
30.62	35.34	197	78	−28	Hofstetter *et al*. (2007)
30.7	35.27	210	86	2	Hofstetter *et al*. (2007)
31.07	35.5	14	84	−19	Hofstetter *et al*. (2007)
31.08	35.44	6	88	−6	Hofstetter *et al*. (2007)
31.08	35.5	359	84	−17	Hofstetter *et al*. (2007)
31.08	35.38	192	86	−8	Hofstetter *et al*. (2007)
31.08	35.45	19	85	−20	Hofstetter *et al*. (2007)
31.09	35.49	5	87	−10.0	Hofstetter *et al*. (2007)
31.09	35.49	209	77	−33	Hofstetter *et al*. (2007)
31.15	35.4	17	73	−40	Hofstetter *et al*. (2007)
31.24	35.37	5	83	−20	Hofstetter *et al*. (2007)
31.24	35.39	13	69	−43	Hofstetter *et al*. (2007)
31.26	35.4	6	85	−15	Hofstetter *et al*. (2007)
31.27	35.47	190	80	170	Salamon *et al*. (2003)
31.3	35.42	7	81	−25	Hofstetter *et al*. (2007)
31.51	35.51	179	69	−51	Hofstetter *et al*. (2007)
31.66	35.49	8	85	−16	Hofstetter *et al*. (2007)
32.2	35.5	175	75	−170	Salamon *et al*. (2003)
32.44	35.25	169	84	−23	Hofstetter *et al*. (2007)
33.85	35.73	200	55	−60	Salamon *et al*. (2003)

an increase of Arabia–Somalia angular velocity occurred sometime after Chron 2A, then it is possible to find a solution that satisfies the observed kinematics of Somalia relative to the surrounding plates. The solution adopted in Table 2 consists into the introduction in the Arabia–Somalia rotation model of an additional stage for the time interval between 1 Ma and the present, with the same Euler pole of anomaly 2A but an increased angular velocity. We determined such an angular velocity by selecting the value that produced the best results along the SWIR, where the azimuth of fracture zones is well constrained. The result listed in Table 2 implies that the angular velocity between Somalia and Arabia has increased from 0.36 to 0.52° Myr^{-1} during the last millions of years. As shown in Fig. 14, the resulting relative motion between Somalia and Nubia along the Main Ethiopian Rift is a slow NW–SE extension, with velocities ranging between 7.7 mm yr^{-1} at the northern triple junction in Afar and 7.1 mm yr^{-1} at 5°N directed N139E. This solution is in excellent agreement with the focal mechanisms calculated for this area (Acocella & Korme 2002; Keir *et al*. 2006; Delvaux & Barth 2010), but it is associated with an Euler pole that is very different from the solutions proposed so far (Chu & Gordon 1999; Fernandes *et al*. 2004; Horner-Johnson *et al*. 2005; Nocquet *et al*. 2006; Vigny *et al*. 2006; Stamps *et al*. 2008; Saria *et al*. 2014). In fact, while our solution implies a clockwise rotation of Somalia with respect to Nubia about an Euler pole located at (27.96°S, 9.67°W), most of these Euler poles coherently range between 25 and 43°E longitude, 27 and 55°S latitude and predict WNW–ESE extension along the Main Ethiopian Rift.

We now consider the Sinai block, whose northern and western boundaries are somewhat less constrained than those of Danakil. Fig. 12 shows published fault plane solutions around Sinai from Salamon *et al*. (2003), Hofstetter *et al*. (2007), the CMT catalogue and EMMA (Vannucci & Gasperini 2004). The areas of strongest seismicity around western Sinai suggest that the known plate boundary associated with the old Gulf of Suez rift (e.g. Bosworth *et al*. 2005) today extends landwards through the Cairo region as indicated in Fig. 12 (e.g. Salamon *et al*. 2003). More to the north, this boundary must link to the Cyprus Trench by a convergent boundary, most likely a diffuse boundary, crossing the eastern Mediterranean. The representative line shown in Fig. 12 was traced using the highest density of seismic activity from the ISC catalogue. The boundary between the Sinai block and Nubia (Fig. 12) is characterized by variable tectonic style and ultraslow motion. It is highly sinistral transtensive along the Gulf of Suez, extensional between the Gulf of Suez and the Cairo region, left-lateral strike–slip as far as the Mediterranean coast of Egypt and convergent in the eastern Mediterranean region. In any case, relative velocity never exceeds 3 mm yr^{-1}, which is compatible with a diffuse plate boundary between the two plates. The simultaneous presence of extensional boundaries to the South and intracontinental convergence to the north suggests that the modern motion of Sinai is mainly driven by friction along the DSFZ, especially along the Lebanese Restraining Bend (e.g. Gomez *et al*. 2006).

5 PLATE RECONSTRUCTIONS SINCE THE EARLY PLIOCENE

A set of plate reconstructions at anomalies 3n.2r (4.62 Ma), 3n (4.18 Ma), 2A (2.58 Ma) and 2 (1.77 Ma) illustrates the plate tectonic evolution of the Red Sea since the early Pliocene (Figs 15 and 16). Figs 15(A) and (B) show plate boundaries and velocity fields during the early Pliocene. At that time, Danakil was rotating with respect to Nubia about a relatively far Euler pole in the central Red Sea and the predicted velocity vectors in Afar are oriented ENE. This motion is similar to the crank-arm rotation envisaged by Sichler (1980), but differs significantly from that model in terms of horizontal gradients of stretching in the Afar region. Apart from this feature, the early Pliocene plate boundaries around Afar appear to be very similar to the present. This is the unique tectonic configuration compatible with both geological and geophysical data during the early Pliocene. In fact, an alternative to the scenario illustrated in Fig. 15(B) could be a configuration where south Danakil belongs to the Arabian plate and the hypothesized HDTZ works as dextral shear zone. In this scenario, the oldest magnetic anomaly crossings along the westernmost segments of the Sheba Ridge would have age decreasing smoothly and continuously from east to west, according to the westward direction of oceanization of the Gulf of Aden. However, Fournier *et al*. (2010) have shown that a gap exists at ∼44°E, where the oldest crossings quite abruptly change from anomaly 5 (10.95 Ma) to anomaly 2A (2.58 Ma). Therefore, the prolongation of the Sheba ridge into Afar cannot be an extensional boundary before 2.58 Ma, because no oceanic crust formed west of ∼44°E before this age and the location of the Euler pole of relative motion between Arabia and Somalia during that stage excludes a transition to a rift zone. Consequently, the westward prolongation of the Sheba Ridge could not be a boundary between Arabia and Somalia, so that the scenario illustrated in Fig. 15(B) is the unique configuration in agreement with both geophysical and geological constraints. A remarkable feature of this reconstruction is represented by the

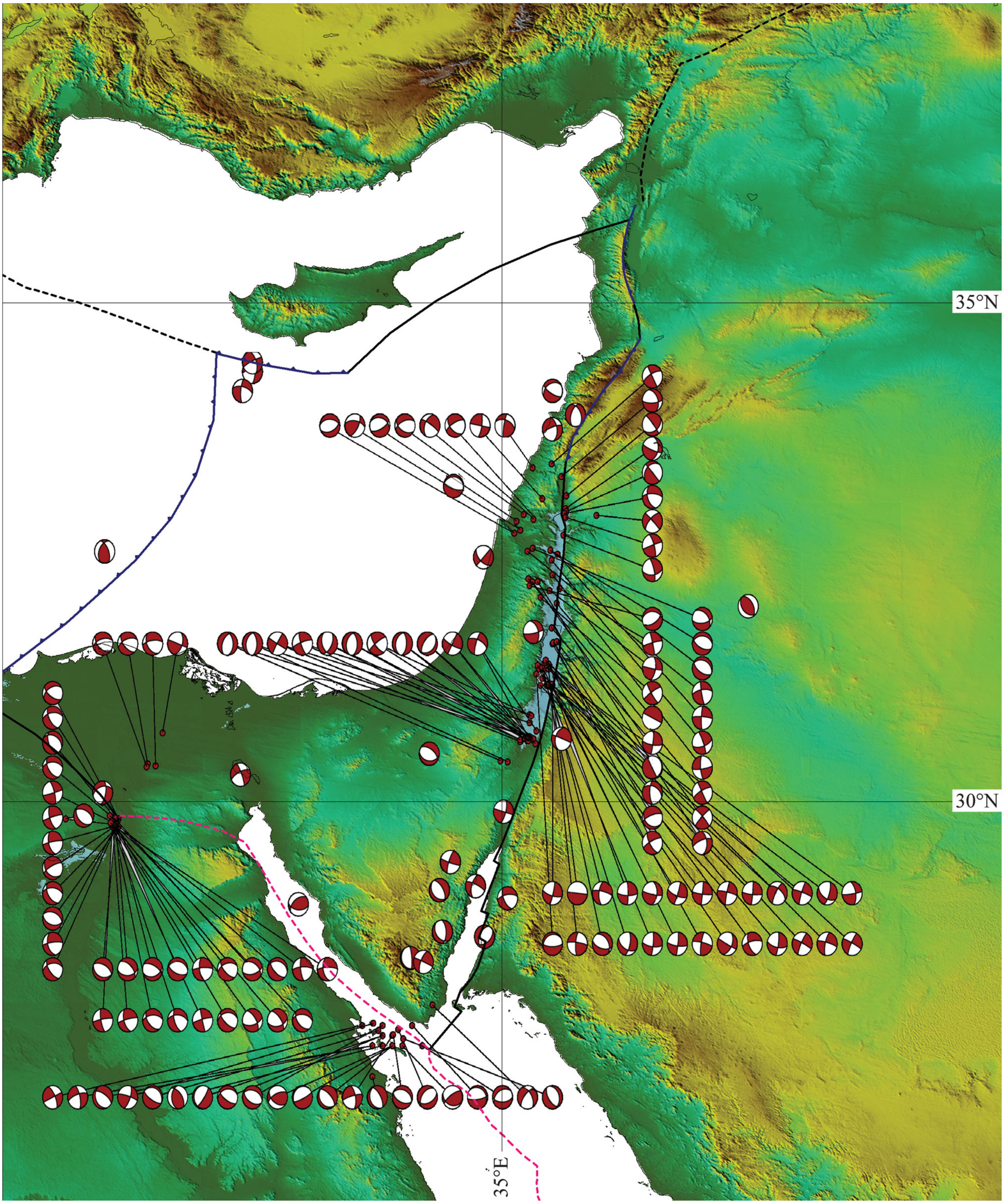

Figure 12. Focal mechanisms of earthquakes around the Sinai block and location and geometry of its representative plate boundaries.

location of the oldest axial cell of seafloor spreading in the Red Sea, which coincides with the location of the rift–rift–rift triple junction between Arabia, Nubia and Danakil. This is exactly what we expect on the basis of geodynamic considerations, because it is likely that the highest extensional strain occurs in the vicinity of a rift–rift–rift triple junction. Let us consider now the early Pliocene configuration in the northern area. Fig. 15(A) shows that at that time the East Anatolian Fault (EAF) was a convergent boundary between Sinai and Eurasia, whereas at present this is mainly a left-lateral strike–slip fault (Fig. 13). All the remaining boundaries in this area maintain the same tectonic style of the early Pliocene reconstruction. The next reconstructions (Figs 15C and D) illustrate plate boundaries

Table 4. Slip rates along the DSFZ.

Method	Slip rate (mm yr^{-1})	Ref
Geological	4 ± 2	Klinger *et al.* (2000)
Seismic moment	5	Jackson & McKenzie (1988)
Geological	4.9 ± 0.2	Ferry *et al.* (2007)
Geological	4.7 ± 1.3	Niemi *et al.* (2001)
GPS	2.6 ± 0.8	Alchalbi *et al.* (2010)
GPS	4.0 ± 0.3	Gomez *et al.* (2007)
GPS	4.9 ± 1.4	Le Beon *et al.* (2008)
GPS	3.7 ± 0.4	Wdowinski *et al.* (2004)
GPS	2.6 ± 1.1	Pe'eri *et al.* (2002)
Geological	3.5 ± 0.2	Bartov & Sagy (2004)
Weighted average	3.9 ± 0.9	This paper

and velocity fields at the time of the oldest magnetic lineation identified in the Red Sea (anomalies 3, 4.18 Ma, early Pliocene). The main difference with respect to the initial scenario of Figs 15(A) and (B) is represented by the northward migration of the Red Sea triple junction and its conversion into a ridge–rift–rift junction. In fact, by the end of chron C3 a linear seafloor spreading segment had formed in the southern Red Sea between Danakil and Arabia. A notable feature of the reconstruction in Fig. 15(D) is that this linear spreading segment is bounded to the south by the unique transverse structure identified in the southern Red Sea. Therefore, the present-day fracture zone shown in Fig. 6 developed from strike–slip faults that separated the area of initial spreading from the southernmost rift region during the early Pliocene, in agreement with the theoretical model of Fig. 2.

Plate reconstructions at anomalies 2A (2.58 Ma, late Pliocene) and 2 (1.77 Ma, early Pleistocene) are illustrated in Figs 16(A) and (B) and (C) and (D), respectively. An important feature of the reconstruction at anomaly 2A is represented by the rapid northward propagation of the Red Sea ridge, while in the southern area it extended by no more than 35 km. Therefore, genuine seafloor spreading started between Nubia and Arabia only at ~2.58 Ma, when the ridge propagated as far as the central region. Finally, a dramatic slowdown occurred during the early Pleistocene at ~1.77 Ma (Figs 16C and D), which determined a partial reorganization of the plate boundaries around the Red Sea. The reconstructions of Figs 16(C) and (D) show that by chron C2 the present-day Euler poles of rotation of Danakil and Sinai with respect to Nubia were established. In the eastern Mediterranean region, the eastern part of the Cyprus Trench was converted into a left-lateral strike–slip boundary that prolonged the EAF.

6 DISCUSSION

The kinematic model illustrated above is mainly based on satellite and marine potential field data. This model illustrates with high detail the plate tectonic evolution of the Red Sea since the early Pliocene. Such initial palaeotectonic scenario is illustrated in Fig. 15 and is compatible with the Afar-Gulf of Aden–southern Red Sea reconstructions of Stab *et al.* (2016). The isochron map of Fig. 10(D) is similar to that of Roeser (1975) and Cochran (1983), but it is founded on a much greater quantity of data, which allowed an accurate estimation of finite reconstruction poles for the last 4.6 Myr. However, the general conclusion of these authors that the first oceanic crust formed in the southern Red Sea around 17.1°N at ~4.6 Ma is confirmed by our analysis. A rigorous determination of plate motions for times older than the late Pliocene was impeded by the absence of anomalies older than 2A between Nubia and Arabia. Consequently, for the time interval between chrons C2A and C3, our model relies on the possibility that the 2–2A stage pole between Nubia and Arabia can be extended backward to anomaly 3. As mentioned above, such assumption is strongly supported by the uniformity of transverse structures across the central and northern Red Sea. With respect to previous kinematic models (e.g. McKenzie *et al.* 1970; Le Pichon & Francheteau 1978; Joffe & Garfunkel 1987; Le Pichon & Gaulier 1988; Jestin *et al.* 1994; Chu & Gordon 1998), the framework proposed in this paper provides a more detailed description of the complex tectonic history of the Danakil microplate and the southern Red Sea.

A comparison of the current plate velocities determined in this study with previous results can be found in Table 5. It shows that our current Arabia–Nubia Euler vector does not differ significantly from the recent GPS results of Reilinger & McClusky (2011). Conversely, it is considerably different with respect to the Euler pole determined by Chu & Gordon's (1998) using exclusively magnetic anomaly crossings. Regarding the Euler poles for Danakil–Arabia, our result is markedly contrasting with both the pole determined by Chu & Gordon's (1998) and the GPS result of McClusky *et al.* (2010). However, the latter is not compatible with the geometry of plate boundaries in the southern Red Sea, because it predicts compression in the Bab–El–Mandeb area (Fig. 11), while it can be shown that the former does not fit the observed trend of shear zones in the southern Red Sea. In Afar, Chu & Gordon's (1998) model predicts a crank-arm rotation of Danakil with respect to Nubia about an Euler pole at 16.3°N, 37.9°E, similar to the pole proposed by Le Pichon & Francheteau (1978). Consequently, they interpret fault plane solutions along the northwestern boundary of Danakil as N–S left-lateral transfer faults that link short extensional segments E–W oriented. Conversely, the model proposed here requires that the same focal mechanisms must be reinterpreted as E–W right-lateral strike–slip, which is as well incompatible with the GPS solution of McClusky *et al.* (2010). In the case of the Sinai block, the flow lines illustrated in Fig. 13 for the Gulf of Suez, which are representative of the Sinai–Nubia relative motion, are in good agreement with the GPS results of McClusky *et al.* (2000), Mahmoud *et al.* (2005) and Riguzzi *et al.* (2006). Finally, the Euler pole of Somalia with respect to Nubia, which is calculated combining our Arabia–Nubia Euler vector with the modified Somalia–Arabia Euler vector of Fournier *et al.* (2010), is markedly contrasting with any other previous determination, but fully satisfies the existing focal mechanisms for the Main Ethiopian Rift (Table 5).

The last point concerns the interpretation of kinematic observations along the DSFZ. Here, we have considered Sinai as an independent block, although its present velocity with respect to Nubia is quite small (Table 2). It is interesting to note that the Sinai–Arabia Euler pole proposed here (Table 5), which is based on earthquake fault plane solutions along the DSFZ, substantially coincides with the Arabia–Nubia Euler pole proposed by Jestin *et al.* (1994) and mainly based on measurements of strike–slip fault azimuths. Although these authors interpreted these data as kinematic indicators for the Arabia–Nubia relative motion, and in fact they assumed that Sinai was fixed to Nubia, the coincidence of the two results supports the reliability of the fit proposed here.

It is interesting to compare the rates of deformation predicted in Afar and northeastern Egypt and Sinai by kinematic models with observed seismic strain rates. Usually, rifting is viewed as a process that generates distributed extensional strain, with a minor component of shearing along transfer faults. However, this view does not take into account that Earth's sphericity introduces a significant component of lateral shear in addition to thinning. In fact,

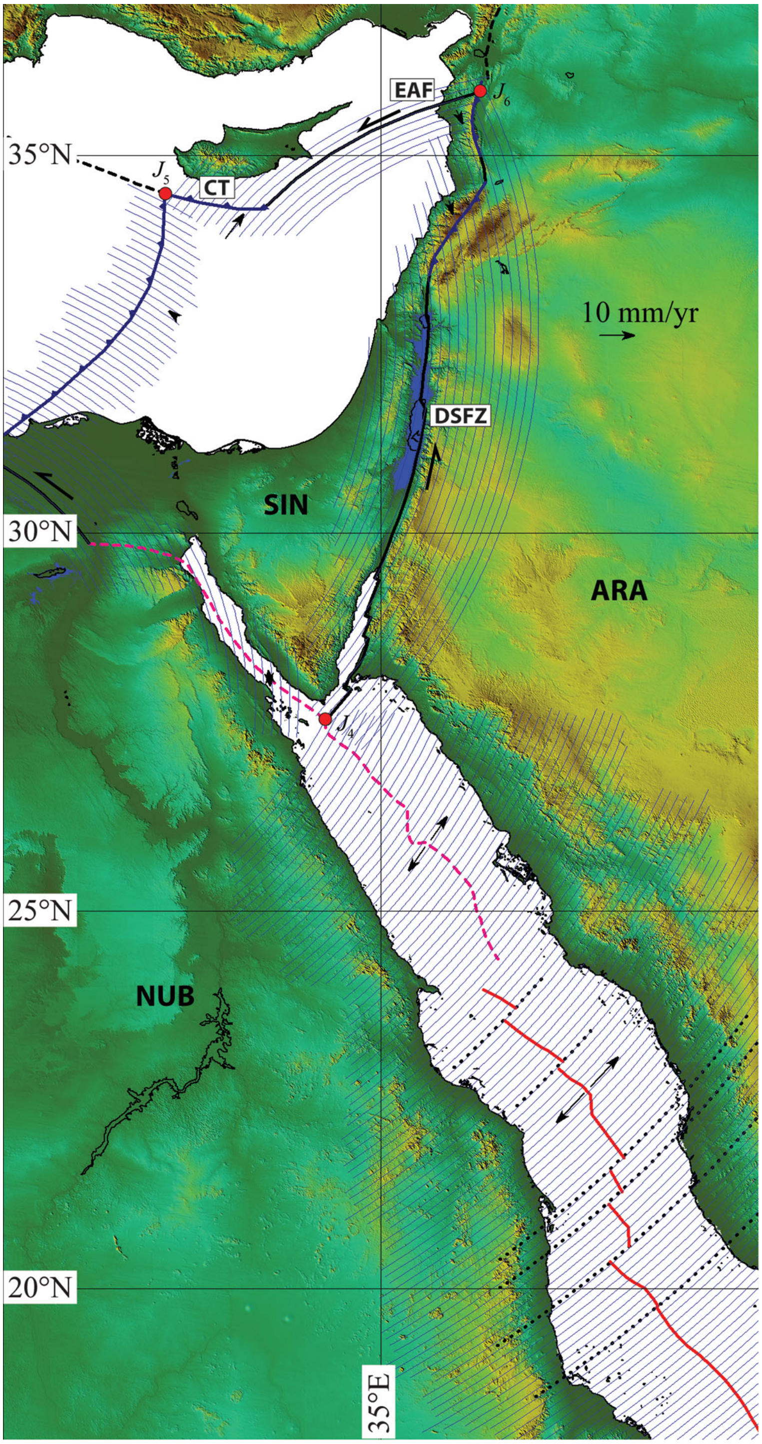

Figure 13. Flow lines and relative velocity field of current plate motions in the northern central Red Sea and in the eastern Mediterranean. CT = Cyprus Trench and EAF = East Anatolian Fault.

two points that were initially close to each other, at the end of the rifting phase have moved apart along a flow line by a distance that depends on how far is the flow line from the Euler pole of relative motion. Consequently, lateral variations of extensional strain can be observed in the deformation zone between the two future plates that move apart, granted that the rifting region is sufficiently close to the Euler pole to induce significant lateral variability. This seems to be the case of Afar, whose distance of a central point from the Nubia–Danakil Euler pole ranges from a minimum of 300 km in the case of Sichler's (1980) pole to 710 km in our determination. The time-averaged shear strain rate associated with lateral variability in extension rates can be easily estimated noting that the linear velocity of extension at distance ζ (in kilometres) from the Euler pole is given by:

$$v(\zeta) = \omega R \sin\left(\frac{\zeta}{R}\right) \tag{3}$$

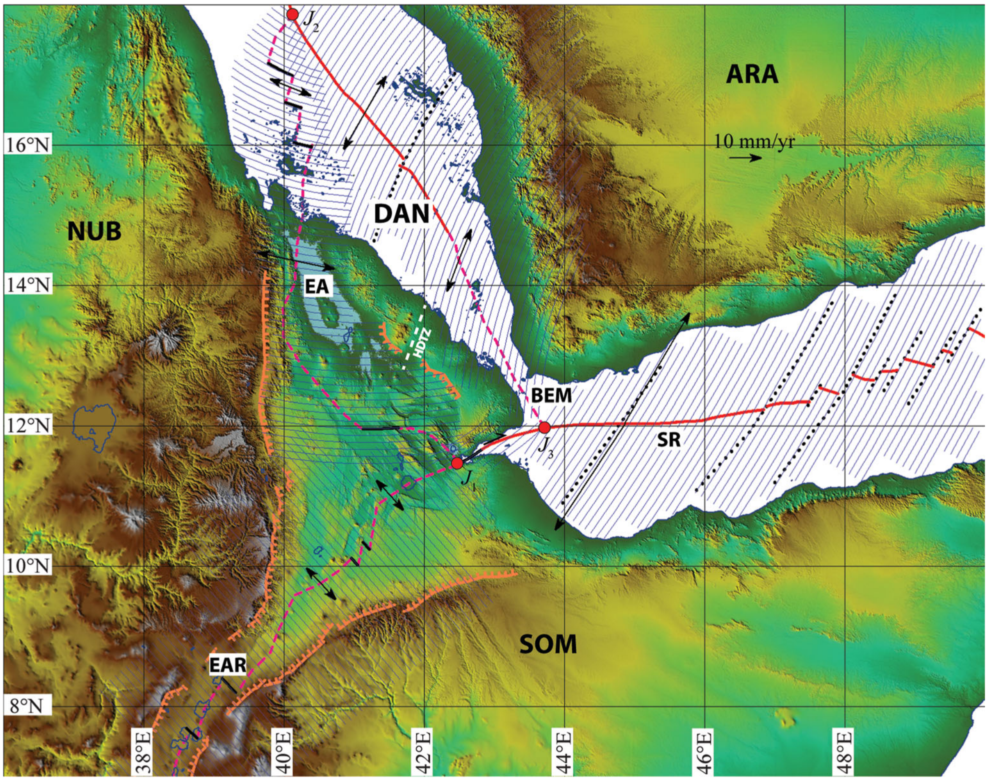

Figure 14. Flow lines and relative velocity field of current plate motions in the southern Red Sea, Afar and in the Gulf of Aden. EA = Erta Ale Rift; BEM = Bab–El–Mandeb and SR = Sheba ridge. HDTZ is the shear zone hypothesized by Barberi & Varet (1977) and Courtillot (1982).

where ω is the average angular velocity about the Euler axis and R is Earth's radius.

Therefore, in a reference frame, where the x and y directions are, respectively, toward the Euler pole and along a flow line, we can estimate the lateral shear strain rate associated with rifting by the expression:

$$\dot{\varepsilon}_{xy} = \frac{1}{2}\frac{\partial v}{\partial \zeta} = \frac{1}{2}\omega \cos\left(\frac{\zeta}{R}\right). \tag{4}$$

This strain rate is small when the rift region lies close to the Euler axis equator, but it increases very rapidly when $\zeta \to 0$. To estimate the local extensional strain rate component, we can apply the following simple formula:

$$\dot{\varepsilon}_{yy} = \frac{\delta L}{L_0} = \frac{\delta L}{L - \delta L} \tag{5}$$

where $\delta L = v(\zeta)\Delta t$ is the distance travelled by a point at distance ζ (in kilometres) from the Euler pole in $\Delta t = 1$ Myr and L is the present-day distance along a small circle arc (flow line) between the unstretched rift shoulders. To compare the rates of extensional and shear deformation in Afar predicted by alternative kinematic models for Danakil–Nubia, we applied expressions (4) and (5) to a central point in Afar using four distinct Euler poles. The results are listed in Table 6. We note that the kinematic strain rates predicted by our model are similar to those that can be inferred on the basis of Chu & Gordon's (1998) model, but significantly lower than those estimated by Sichler's (1980) model and McClusky's *et al.* (2010) GPS observations. Table 6 also shows a comparison of the kinematic strain rates with seismic strain rates that are calculated applying Kostrov's (1974) formula to a compilation of focal mechanisms for the Afar region (Table S1 in Supporting Information). To this purpose, we used the following expression:

$$\dot{\varepsilon}_{ij} = \frac{\langle \dot{M}_0 \rangle}{2\mu V} \sum_k m_{ij}^{(k)} \tag{6}$$

where $\langle \dot{M}_0 \rangle$ is the average annual rate of scalar seismic moment release, μ is the rigidity modulus, V is the volume of the deforming region and m_{ij} are components of the geometrical part of the moment tensor (Aki & Richards 2002). The sum was extended to all the seismic events included in Table S1 in the Supporting Information. To estimate the annual rate of seismic moment release, we used a simple power-law distribution (e.g. Molnar 1979). In this instance, the annual number of earthquakes with seismic moment greater than or equal to an assigned value M_0 in the deforming region is given by:

$$N(M_0) = \alpha M_0^{-\beta}. \tag{7}$$

In this expression, α and β are constants that can be determined statistically, analogue to the classic Gutenberg–Richter constants a and b. Theoretical arguments suggest that β is close to 0.5 for any specific tectonic region (e.g. Kagan 1991). From a least-squares fit of the theoretical distribution to the observed seismic moment release in Afar, we obtained: $\alpha = 2.1113 \times 10^{+9}$ $[\mathrm{N\,m}]^{\beta}$ yr^{-1} and $\beta = 0.5675$, which is close to the theoretical value of 0.5. Starting from (7), Molnar (1979) proved that the average annual rate of scalar seismic moment release, $\langle \dot{M}_0 \rangle$, can be estimated by the following simple expression:

$$\langle \dot{M}_0 \rangle = \frac{\alpha}{1-\beta} M_{0,\max}^{1-\beta} \tag{8}$$

where $M_{0,\max}$ is the maximum observed seismic moment. Using the values of α and β obtained above and the data listed in

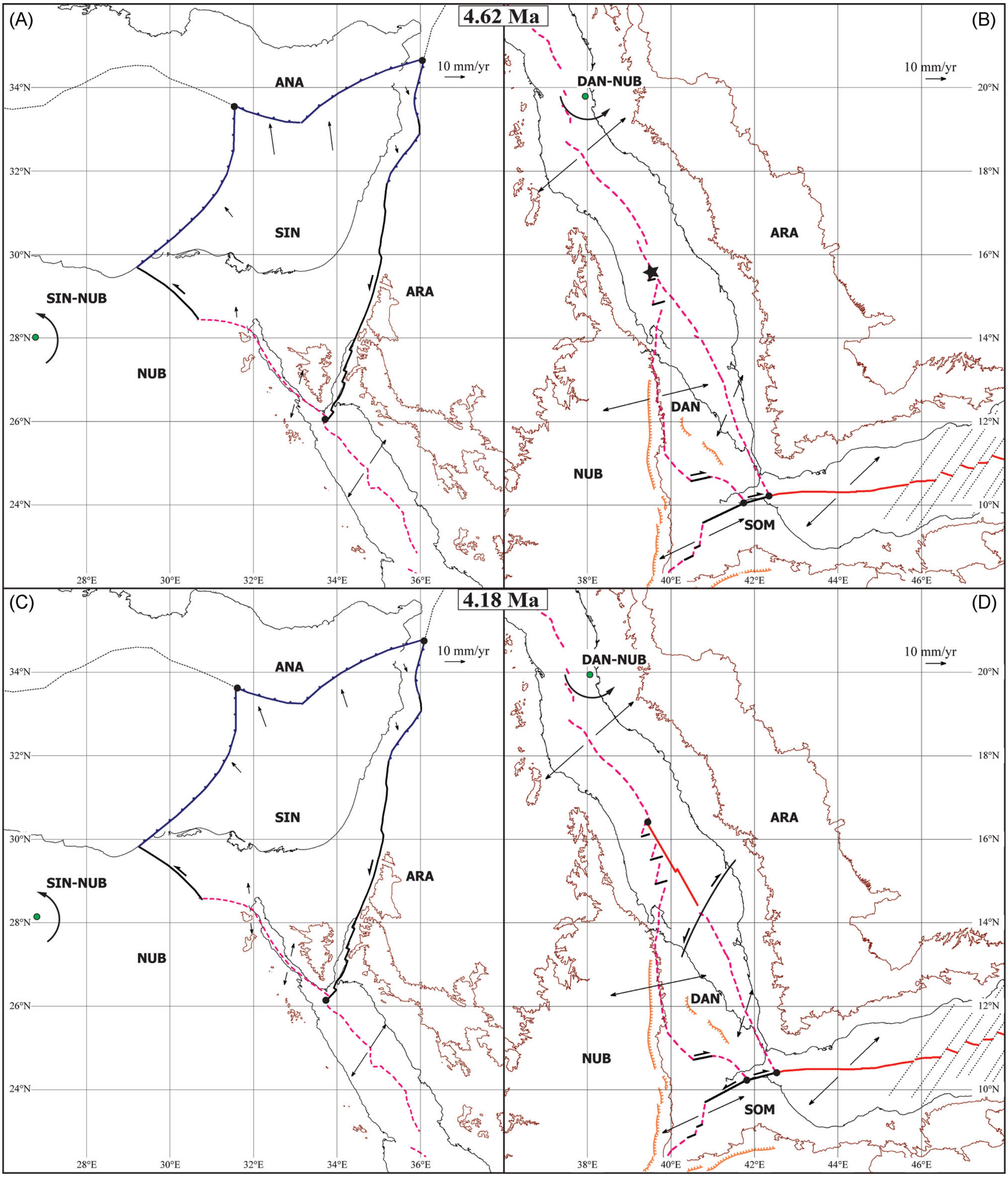

Figure 15. Plate reconstructions at chron C3n.2ry (4.62 Ma) for the northern Red Sea and eastern Mediterranean (A) and for the southern Red Sea, Afar and western Gulf of Aden (B), showing past plate boundaries and velocity vectors of relative motion. Also shown are instantaneous Euler poles of Sinai–Nubia and Danakil–Nubia plate pairs. The star in (B) indicates the reconstructed location of the first oceanic crust formed in the southern Red Sea, which coincides with the Danakil–Nubia–Arabia triple junction. Black dots are triple junctions. Red solid lines: mid-ocean ridges; red dashed lines: rift axes; black dotted lines: fracture zones and transform faults; black solid lines: strike–slip faults; blue lines with triangular barbs: convergent boundaries; orange lines with squared barbs: major rift structures and brown lines: reconstructed modern 1000 m topographic contour. Panels (C) and (D) show plate reconstructions at chron C3n (4.18 Ma) for the same regions.

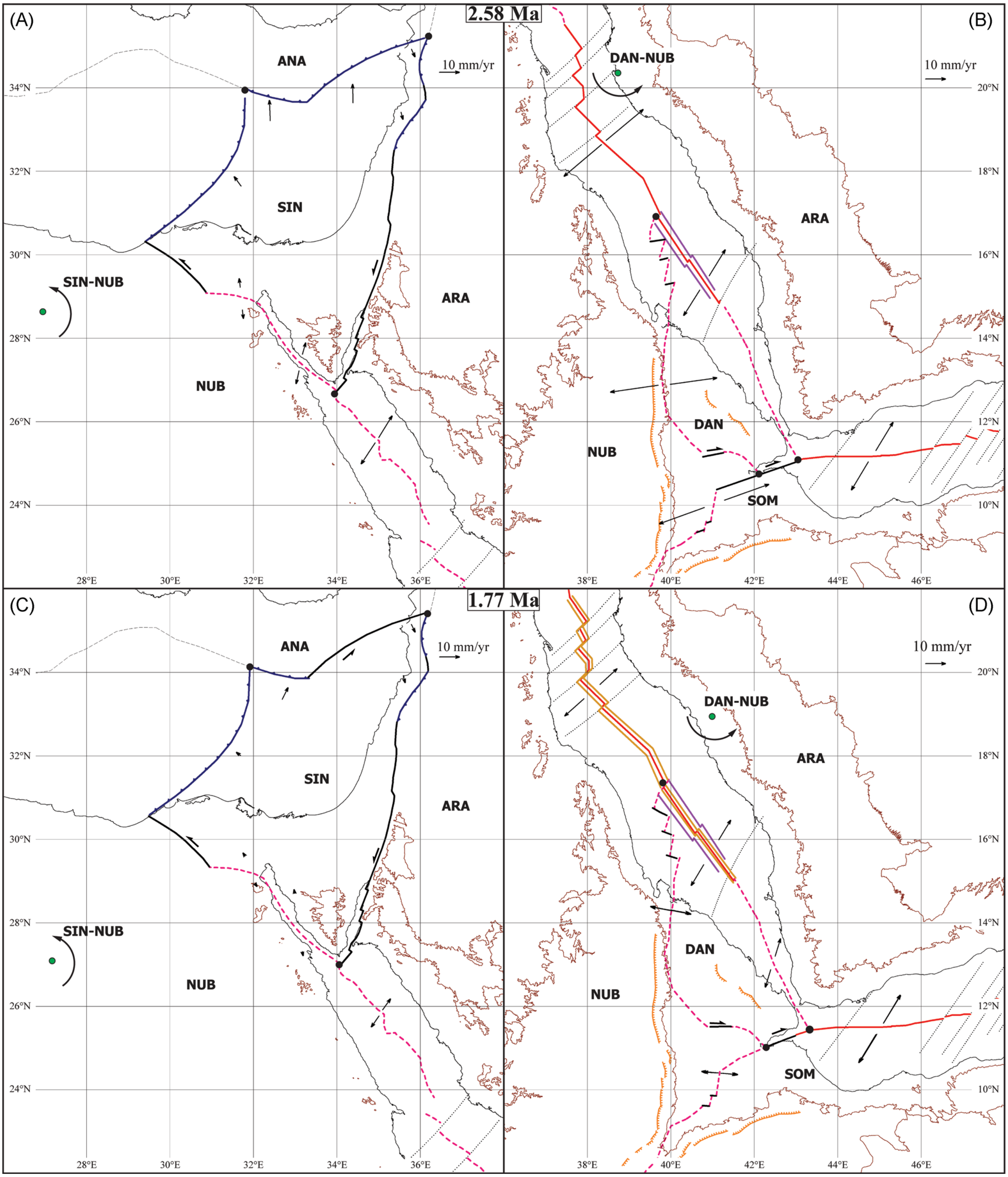

Figure 16. Plate reconstructions at the end of chron C2A (2.58 Ma) for the northern Red Sea and eastern Mediterranean (A) and for the southern Red Sea, Afar and western Gulf of Aden (B). Purple lines: isochrons 3; other symbols are the same of Fig. 15. Panels (C) and (D) show plate reconstructions at chron C2n (1.77 Ma) for the same regions. Ocra lines: isochrons 2A.

Table S1 in the Supporting Information, in the case of Afar we found: $\langle \dot{M}_0 \rangle = 6.94 \times 10^{17}$ N m yr^{-1}. A surprising feature of the seismic strain rates listed in Table 6 is that they are considerably greater than the corresponding kinematic rates. In particular, shear and extensional strain rates are, respectively, one order of magnitude and 3–4 times higher than those predicted by kinematic models. Although this result deserves further study, for the moment we can reasonably assume that a major component of the deformation in

Table 5. Current Euler vectors for the Arabia–Nubia–Somalia–Danakil–Sinai five-plates system.

λ (°)	ϕ (°)	ω (° Myr^{-1})	Technique	References
			Arabia–Nubia	
30.32	27.18	0.49	MMA	This paper
30.5	25.7	0.37	GPS	McClusky *et al.* (2003)
31.5	23.0	0.421	MMA	Chu & Gordon (1998)
31.64	20.29	0.308	GPS	Vigny *et al.* (2006)
32.39	31.66	0.50	DORIS–GPS	Nocquet *et al.* (2006)
31.7	24.6	0.369	GPS	ArRajehi *et al.* (2010)
31.5	25.2	0.393	GPS	Reilinger & McClusky (2011)
			Somalia–Nubia	
27.96	170.33	0.08	Calculated	This paper
54.76	216.97	0.069	GPS	Fernandes *et al.* (2004)
28.95	223.70	0.084	Calculated	Vigny *et al.* (2006)
40.78	205.46	0.06	DORIS–GPS	Nocquet *et al.* (2006)
27.30	216.20	0.089	Calculated	Chu & Gordon (1999)
34.44	217.81	0.065	GPS	Saria *et al.* (2014)
44.70	182.80	0.084	Calculated	Horner-Johnson *et al.* (2005)
			Arabia–Somalia	
23.67	22.21	0.364	MMA	Fournier *et al.* (2010)
20.07	25.49	0.356	GPS	Vigny *et al.* (2006)
22.0	26.2	0.404	GPS	ArRajehi *et al.* (2010)
			Danakil–Nubia	
19.55	41.30	1.16	Calculated	This paper
16.3	37.9	1.276	Calculated	Chu & Gordon (1998)
17.0	39.7	1.9	GPS	McClusky *et al.* (2010)
			Danakil–Arabia	
11.68	49.74	0.71	MMA	This paper
8.9	43.9	0.893	MMA	Chu & Gordon (1998)
13.4	42.9	1.5	GPS	McClusky *et al.* (2010)
			Sinai–Nubia	
27.62	27.38	0.21	Calculated	This paper
			Sinai–Arabia	
–32.37	207.02	0.28	Seismic slip	This paper
–35.7	197.1	0.154	GPS	ArRajehi *et al.* (2010)

Notes: λ,ϕ are the geographic coordinates (lat,lon) of the Euler pole.
ω is the counterclockwise angular velocity.
MMA = marine magnetic anomalies.

Table 7. Comparison between seismic and kinematic extensional/shear strain rates along the western Sinai–Gulf of Suez–northeastern Egypt rift zone.

	Kinematic	Seismic
$\dot{\varepsilon}_{yy}$ (s^{-1})	3.27E–16	2.91±0.03E–16
$\dot{\varepsilon}_{yx}$ (s^{-1})	5.79E–17	5.39±0.01E–16

Afar is associated with the stress field generated by the Afar plume and with the transient creep induced by continued magmatic injection (e.g. Nooner *et al*. 2009).

The method discussed above was also applied to the western Sinai–Gulf of Suez–northeastern Egypt rift zone, which is part of the Nubia– Sinai plate boundary. A comparison between the kinematic and seismic rates of extensional and shear deformation is listed in Table 7. In this instance, the kinematic strain rate was calculated using the Euler vector of Sinai–Nubia (Table 5), while a compilation of earthquake focal mechanisms for this region can be found in Table S2 of the Supporting Information. We first note that all the quantities listed in Table 7 are one order of magnitude smaller than the corresponding quantities for the Afar region. There is good agreement between kinematic and seismic extensional strain rates, whereas the predicted kinematic shear strain is also in this case one order of magnitude smaller than the observed seismic strain rate. Such a discrepancy cannot be explained by magmatic activity and requires further investigation.

7 CONCLUSIONS

In this paper, we have addressed the problem of describing plate motions in the Red Sea region through a detailed analysis of long-term geological and geophysical data and standard plate kinematic modelling. Integration of several sources of data was an important step of our procedure, not only because a single data set did not allow a reliable reconstruction of the tectonic history of this region back to the late Miocene, but especially for the reciprocal capability of individual data sets to assess data coming from other sources. In general, the leading principle of our analysis was the idea that the structural pattern of deformation in the extending region between two plates that are moving apart is constrained primarily by the flow lines of relative motion. The isochron map obtained by the analysis of marine magnetic anomalies and fracture zone trends describes accurately the history of oceanization of the Red Sea since the early Pliocene (~4.62 Ma). We have also shown that the location of the oldest oceanic crust in the southern Red Sea coincides with a fossil rift–rift–rift triple junction between Arabia, Nubia and Danakil. Finally, an important result of the plate reconstructions discussed above is that the unique fracture zone identified in the southern Red Sea bounds to the south the oldest linear spreading segment formed in this region, thereby confirming the model of formation of continent–continent fracture zones proposed here.

ACKNOWLEDGEMENTS

This work was funded by the MIUR, PRIN prot. 20125JKANY. The GEODAS ship-track data used in this study can be found at NGDC (http://www.ngdc.noaa.gov/mgg/geodas/trackline.html). The computer program used in the analysis of magnetic data was designed by the first author and can be freely downloaded at: http://www.serg.unicam.it/Downloads.htm. We thank two anonymous reviewers for their useful suggestions that improved the manuscript.

REFERENCES

Acocella, V. & Korme, T., 2002. Holocene extension direction along the main Ethiopian Rift, East Africa, *Terra Nova*, **14**(3), 191–197.

Aki, K. & Richards, P.G., 2002. *Quantitative Seismology*, 2nd edn, University Science Books, 700 pp.

Table 6. Comparison between seismic and kinematic extensional/shear strain rates in Afar.

	This paper	S80	CG98	MC10	Seismic
$\dot{\varepsilon}_{yy}$ (s^{-1})	1.77E–15	2.15E–15	1.47E–15	2.06E–15	6.54±0.21E–15
$\dot{\varepsilon}_{yx}$ (s^{-1})	3.19E–16	7.60E–16	3.52E–16	5.25E–16	4.49±0.22E–15

Notes: S80 = Sichler (1980); CG98 = Chu & Gordon (1998); McClusky *et al.* (2010).

Al-Amri, A.M.S., Punsalan, B.T. & Uy, E.A., 1998. Spatial distribution of the seismicity parameters in the Red Sea regions, *J. Asian Earth Sci.*, **16**(5), 557–563.

Alchalbi, A. *et al.*, 2010. Crustal deformation in northwestern Arabia from GPS measurements in Syria: slow slip rate along the northern Dead Sea Fault, *Geophys. J. Int.*, **180**(1), 125–135.

Al-Saud, M.M., 2008. Seismic characteristics and kinematic models of Makkah and central Red Sea regions, *Arab. J. Geosci.*, **1**(1), 49–61.

ArRajehi, A. *et al.*, 2010. Geodetic constraints on present-day motion of the Arabian Plate: implications for Red Sea and Gulf of Aden rifting, *Tectonics*, **29**, TC3011, doi:10.1029/2009TC002482.

Badawy, A., 2005. Present-day seismicity, stress field and crustal deformation of Egypt, *J. Seismol.*, **9**(3), 267–276.

Badawy, A. & Horváth, F., 1999. The Sinai subplate and tectonic evolution of the northern Red Sea region, *J. Geodyn.*, **27**(4), 433–450.

Barberi, F. & Varet, J., 1977. Volcanism of Afar: small-scale plate tectonics implications. *Bull. geol. Soc. Am.*, **88**(9), 1251–1266.

Bartov, Y. & Sagy, A., 2004. Late Pleistocene extension and strike-slip in the Dead Sea Basin, *Geol. Mag.*, **141**(05), 565–572.

Bellahsen, N., Husson, L., Autin, J., Leroy, S. & d'Acremont, E., 2013. The effect of thermal weakening and buoyancy forces on rift localization: field evidences from the Gulf of Aden oblique rifting, *Tectonophysics*, **607**, 80–97.

Bonatti, E., 1985. Punctiform initiation of seafloor spreading in the Red Sea during transition from continental to an oceanic rift, *Nature*, **316**, 33–37.

Bosworth, W., Huchon, P. & McClay, K., 2005. The Red Sea and Gulf of Aden basins, *J. Afr. Earth Sci.*, **43**(1), 334–378.

Cande, S.C. & Kent, D.V., 1995. Revised calibration of the geomagnetic polarity timescale for the late Cretaceous and Cenozoic, *J. geophys. Res.*, **100**(B4), 6093–6095.

Chu, D. & Gordon, R.G., 1998. Current plate motions across the Red Sea, *Geophys. J. Int.*, **135**(2), 313–328.

Chu, D. & Gordon, R.G., 1999. Evidence for motion between Nubia and Somalia along the Southwest Indian Ridge, *Nature*, **398**(6722), 64–67.

Cochran, J.R., 1983. A model for development of Red Sea, *AAPG Bull.*, **67**(1), 41–69.

Collet, B., Taud, H., Parrot, J.F., Bonavia, F. & Chorowicz, J., 2000. A new kinematic approach for the Danakil block using a Digital Elevation Model representation, *Tectonophysics*, **316**(3), 343–357.

Courtillot, V., 1982. Propagating rifts and continental breakup, *Tectonics*, **1**(3), 239–250.

Courtillot, V., Achache, J., Landre, F., Bonhommet, N., Montigny, R. & Féraud, G., 1984. Episodic spreading and rift propagation: new paleomagnetic and geochronologic data from the Afar Nascent passive margin, *J. geophys. Res.*, **89**(B5), 3315–3333.

d'Acremont, E., Leroy, S., Beslier, M.-O., Bellahsen, N., Fournier, M., Robin, C., Maia, M. & Gente, P., 2005. Structure and evolution of the eastern Gulf of Aden conjugate margins from seismic reflection data, *Geophys. J. Int.*, **160**, 869–890.

Dahy, S.A., 2010. A study on seismicity and tectonic setting in the northeastern part of Egypt, *Res. J. Earth Sci.*, **2**(1), 8–13.

Delvaux, D. & Barth, A., 2010. African stress pattern from formal inversion of focal mechanism data, *Tectonophysics*, **482**(1), 105–128.

DeMets, C. & Wilson, D.S., 2008. Toward a minimum change model for recent plate motions: calibrating seafloor spreading rates for outward displacement, *Geophys. J. Int.*, **174**(3), 825–841.

Eagles, G., Gloaguen, R. & Ebinger, C., 2002. Kinematics of the Danakil microplate, *Earth planet. Sci. Lett.*, **203**(2), 607–620.

Fernandes, R.M.S., Ambrosius, B.A.C., Noomen, R., Bastos, L., Combrinck, L., Miranda, J.M. & Spakman, W., 2004. Angular velocities of Nubia and Somalia from continuous GPS data: implications on present-day relative kinematics, *Earth planet. Sci. Lett.*, **222**(1), 197–208.

Ferry, M., Meghraoui, M., Karaki, N.A., Al-Taj, M., Amoush, H., Al-Dhaisat, S. & Barjous, M., 2007. A 48-kyr-long slip rate history for the Jordan Valley segment of the Dead Sea Fault, *Earth planet. Sci. Lett.*, **260**(3), 394–406.

Fnais, M., Al-Amri, A., Abdelrahman, K., Abdelmonem, E. & El-Hady, S., 2015. Seismicity and seismotectonics of Jeddah-Makkah Region, West-Central Saudi Arabia, *J. Earth Sci.*, **26**(5), 746–754.

Fournier, M. *et al.*, 2010. Arabia-Somalia plate kinematics, evolution of the Aden-Owen-Carlsberg triple junction, and opening of the Gulf of Aden, *J. geophys. Res.*, **115**, B04102, doi:10.1029/2008JB006257.

Ghebreab, W., 1998. Tectonics of the Red Sea region reassessed, *Earth Sci. Rev.*, **45**(1), 1–44.

Gomez, F., Khawlie, M., Tabet, C., Nasser Darkal, A., Khair, K. & Barazangi, M., 2006. Late Cenozoic uplift along the northern Dead Sea transform in Lebanon and Syria, *Earth planet. Sci. Lett.*, **241**(3), 913–931.

Gomez, F. *et al.*, 2007. Global Positioning System measurements of strain accumulation and slip transfer through the restraining bend along the Dead Sea fault system in Lebanon, *Geophys. J. Int.*, **168**(3), 1021–1028.

Hellinger, S.J., 1981. The uncertainties of finite rotations in plate tectonics, *J. geophys. Res.*, **86**, 9312–9318.

Hofstetter, R., Klinger, Y., Amrat, A.Q., Rivera, L. & Dorbath, L., 2007. Stress tensor and focal mechanisms along the Dead Sea fault and related structural elements based on seismological data, *Tectonophysics*, **429**(3), 165–181.

Horner-Johnson, B.C., Gordon, R.G., Cowles, S.M. & Argus, D.F., 2005. The angular velocity of Nubia relative to Somalia and the location of the Nubia–Somalia–Antarctica triple junction, *Geophys. J. Int.*, **162**(1), 221–238.

Hosny, A., Omar, K. & Ali, S.M., 2013. The Gulf of Suez earthquake, 30 January 2012, northeast of Egypt, *Rend. Lincei*, **24**(4), 377–386.

Hussein, H.M., Marzouk, I., Moustafa, A.R. & Hurukawa, N., 2006. Preliminary seismicity and focal mechanisms in the southern Gulf of Suez: August 1994 through December 1997, *J. Afr. Earth Sci.*, **45**(1), 48–60.

Izzeldin, A.Y., 1989. Transverse structures in the central part of the Red Sea and implications on early stages of oceanic accretion, *Geophys. J. Int.*, **96**(1), 117–129.

Jackson, J. & McKenzie, D., 1988. The relationship between plate motions and seismic moment tensors, and the rates of active deformation in the Mediterranean and Middle East, *Geophys. J. Int.*, **93**(1), 45–73.

Jestin, F., Huchon, P. & Gaulier, J.M., 1994. The Somalia plate and the East African Rift System: present-day kinematics, *Geophys. J. Int.*, **116**(3), 637–654.

Joffe, S. & Garfunkel, Z., 1987. Plate kinematics of the circum Red Sea—a re-evaluation, *Tectonophysics*, **141**(1), 5–22.

Kagan, Y.Y., 1991. Seismic moment distribution, *Geophys. J. Int.*, **106**, 123–134.

Keir, D., Ebinger, C.J., Stuart, G.W., Daly, E. & Ayele, A., 2006. Strain accommodation by magmatism and faulting as rifting proceeds to breakup: seismicity of the northern Ethiopian rift, *J. geophys. Res.*, **111**(B5), B05314, doi:10.1029/2005JB003748.

Klinger, Y., Avouac, J.P., Karaki, N.A., Dorbath, L., Bourles, D. & Reyss, J.L., 2000. Slip rate on the Dead Sea transform fault in northern Araba valley (Jordan), *Geophys. J. Int.*, **142**(3), 755–768.

Korostelev, F. *et al.*, 2015. Upper mantle structure of the southern Arabian margin: insights from teleseismic tomography, *Geosphere*, **11**(5), 1262–1278.

Korostelev, F. *et al.*, 2016. Magmatism at continental passive margins inferred from Ambient-Noise Phase-velocity in the Gulf of Aden, *Terra Nova*, **28**(1), 19–26.

Kostrov, V.V., 1974. Seismic moment and energy of earthquakes, and seismic flow of rock, *Izv. Acad. Sci. USSR Phys. Solid Earth*, **1**, 23–44.

Le Beon, M. *et al.*, 2008. Slip rate and locking depth from GPS profiles across the southern Dead Sea Transform, *J. geophys. Res.*, **113**, B11403, doi:10.1029/2007JB005280.

Le Pichon, X. & Francheteau, J., 1978. A plate-tectonic analysis of the Red Sea–Gulf of Aden area, *Tectonophysics*, **46**, 369–406.

Le Pichon, X.T. & Gaulier, J.M., 1988. The rotation of Arabia and the Levant fault system, *Tectonophysics*, **153**(1), 271–294.

Leroy, S. *et al.*, 2010. Contrasted styles of rifting in the eastern Gulf of Aden: a combined wide-angle, multichannel seismic, and heat flow survey, *Geochem. Geophys. Geosyst.*, **11**(7), Q07004, doi:10.1029/2009GC002963.

Leroy, S. *et al.*, 2012. From rifting to oceanic spreading in the Gulf of Aden: a synthesis, *Arab J. Geosci.*, **5**(5), 859–901.

Ligi, M. *et al.*, 2011. Initial burst of oceanic crust accretion in the Red Sea due to edge-driven mantle convection, *Geology*, **391**(11), 1019–1022.

Ligi, M. *et al.*, 2012. Birth of an Ocean in the Red Sea: initial pangs, *Geochem. Geophys. Geosyst.*, **13**(8), 1–29.

Lucazeau, F. *et al.*, 2008. Persistent thermal activity at the Eastern Gulf of Aden after continental break-up, *Nat. Geosci.*, **1**(12), 854–858.

Mahmoud, S., Reilinger, R., McClusky, S., Vernant, P. & Tealeb, A., 2005. GPS evidence for northward motion of the Sinai Block: implications for E. Mediterranean tectonics, *Earth planet. Sci. Lett.*, **238**(1), 217–224.

Makris, J. & Rihm, R., 1991. Shear-controlled evolution of the Red Sea: pull apart model, *Tectonophysics*, **198**(2), 441–466.

Manighetti, I., Tapponnier, P., Courtillot, V., Gallet, Y., Jacques, E. & Gillot, P.-Y., 2001. Strain transfer between disconnected, propagating rifts in Afar, *J. geophys. Res.*, **106**(B7), 13 613–13 665.

Matias, L.M., Olivet, J.L., Aslanian, D. & Fidalgo, L., 2005. PLACA: a white box for plate reconstruction and best-fit pole determination, *Comput. Geosci.*, **31**(4), 437–452.

McClusky, S., Reilinger, R., Mahmoud, S., Ben Sari, D. & Tealeb, A., 2003. GPS constraints on Africa (Nubia) and Arabia plate motions, *Geophys. J. Int.*, **155**(1), 126–138.

McClusky, S. *et al.*, 2000. Global Positioning System constraints on plate kinematics and dynamics in the eastern Mediterranean and Caucasus, *J. geophys. Res.*, **105**(B3), 5695–5719.

McClusky, S. *et al.*, 2010. Kinematics of the southern Red Sea–Afar Triple Junction and implications for plate dynamics, *Geophys. Res. Lett.*, **37**, L05301, doi:10.1029/2009GL041127.

McKenzie, D.P., Davies, D. & Molnar, P., 1970. Plate tectonics of the Red Sea and East Africa, *Nature*, **226**(5242), 243–248.

Molnar, P., 1979. Earthquake recurrence intervals and plate tectonics, *Bull. seism. Soc. Am.*, **69**(1), 115–133.

Niemi, T.M., Zhang, H., Atallah, M. & Harrison, J.B.J., 2001. Late Pleistocene and Holocene slip rate of the northern Wadi Araba fault, Dead Sea transform, Jordan, *J. Seismol.*, **5**(3), 449–474.

Nocquet, J.M., Willis, P. & Garcia, S., 2006. Plate kinematics of Nubia–Somalia using a combined DORIS and GPS solution, *J. Geod.*, **80**(8–11), 591–607.

Nooner, S.L., Bennati, L., Calais, E., Buck, W.R., Hamling, I.J., Wright, T.J. & Lewi, E., 2009. Post-rifting relaxation in the Afar region, Ethiopia, *Geophys. Res. Lett.*, **36**, L21308, doi:10.1029/2009GL040502.

Pallister, J.S., 1986. Explanatory notes to the geologic map of the Al Lith quadrangle, sheet 20D, Saudi Arabian Deputy Ministry for Mineral Resources Map Series, Kingdom of Saudi Arabia, 143 p., 2 sheets, scale 1:250 000.

Pallister, J.S., 1987. Magmatic history of Red Sea rifting: perspective from the central Saudi Arabian coastal plain, *Bull. geol. Soc. Am.*, **98**(4), 400–417.

Pe'eri, S., Wdowinski, S., Shtibelman, A., Bechor, N., Bock, Y., Nikolaidis, R. & van Domselaar, M., 2002. Current plate motion across the Dead Sea Fault from three years of continuous GPS monitoring, *Geophys. Res. Lett.*, **29**(14), doi:10.1029/2001GL013879.

Reilinger, R. & McClusky, S., 2011. Nubia–Arabia–Eurasia plate motions and the dynamics of Mediterranean and Middle East tectonics, *Geophys. J. Int.*, **186**(3), 971–979.

Riguzzi, F., Pietrantonio, G., Piersanti, A. & Mahmoud, S.M., 2006. Current motion and short-term deformations in the Suez–Sinai area from GPS observations, *J. Geodyn.*, **41**(5), 485–499.

Roeser, H.A., 1975. A detailed magnetic survey of the southern Red Sea, *Geol. Jahrbuch*, **13**, 131–153.

Salamon, A., Hofstetter, A., Garfunkel, Z. & Ron, H., 2003. Seismotectonics of the Sinai subplate—the eastern Mediterranean region, *Geophys. J. Int.*, **155**(1), 149–173.

Sandwell, D.T., Müller, R.D., Smith, W.H., Garcia, E. & Francis, R., 2014. New global marine gravity model from CryoSat-2 and Jason-1 reveals buried tectonic structure, *Science*, **346**(6205), 65–67.

Saria, E., Calais, E., Stamps, D.S., Delvaux, D. & Hartnady, C.J.H., 2014. Present-day kinematics of the East African Rift, *J. geophys. Res.*, **119**, doi:10.1002/2013JB010901.

Schettino, A., 2012. Magan: a new approach to the analysis and interpretation of marine magnetic anomalies, *Comput. Geosci.*, **39**, 135–144.

Schettino, A. & Macchiavelli, C., 2016. Plate kinematics of the central Atlantic during the Oligocene and Early Miocene, *Geophys. J. Int.*, **205**, 395–413.

Schlische, R.W., Withjack, M.O. & Olsen, P.E., 2003. Relative timing of CAMP, rifting, continental breakup, and basin inversion: tectonic significance, in *The Central Atlantic Magmatic Province: Insights from Fragments of Pangea*, eds Hames, W., Mchone, J.G., Renne, P. & Ruppel, C., American Geophysical Union, doi:10.1029/136GM03.

Sichler, B., 1980. La biellette danakile: Un modèle pour l'évolution géodynamique de l'Afar, *Bull. Soc. Géol. Fr.*, **22**(6), 925–932.

Souriot, T. & Brun, J.P., 1992. Faulting and block rotation in the Afar triangle, East Africa: the Danakil "crank-arm" model, *Geology*, **20**(10), 911–914.

Stab, M., Bellahsen, N., Pik, R., Quidelleur, X., Ayalew, D. & Leroy, S., 2016. Modes of rifting in magma-rich settings: tectono-magmatic evolution of Central Afar, *Tectonics*, **35**, 2–38.

Stamps, D.S., Calais, E., Saria, E., Hartnady, C., Nocquet, J.-M., Ebinger, C.J. & Fernandes, R.M., 2008. A kinematic model for the East African Rift, *Geophys. Res. Lett.*, **35**, L05304, doi:10.1029/2007GL032781.

Talwani, M. & Abreu, V., 2000. Inferences regarding initiation of oceanic crust formation from the U.S. East Coast Margin and Conjugate South Atlantic Margins, in *Atlantic Rifts and Continental Margins*, Geophysical Monograph, Vol. 115, pp. 211–233, eds Mohriak, W. & Talwani, M., American Geophysical Union.

Vannucci, G. & Gasperini, P., 2004. The new release of the database of Earthquake Mechanisms of the Mediterranean Area (EMMA Version 2), *Ann. Geophys.*, **47**(Suppl.), 307–334.

Vigny, C., Huchon, P., Ruegg, J.-C., Khanbari, K. & Asfaw, L.M., 2006. Confirmation of Arabia plate slow motion by new GPS data in Yemen, *J. geophys. Res.*, **111**, B02402, doi:10.1029/2004JB003229.

Wdowinski, S. *et al.*, 2004. GPS measurements of current crustal movements along the Dead Sea Fault, *J. geophys. Res.*, **109**, B05403, doi:10.1029/2003JB002640.

Withjack, M.O., Olsen, P.E. & Schlische, R.W., 1995. Tectonic evolution of the Fundy rift basin, Canada: evidence of extension and shortening during passive margin development, *Tectonics*, **14**(2), 390–405.

Wolfenden, E., Ebinger, C., Yirgu, G., Deino, A. & Ayalew, D., 2004. Evolution of the northern Main Ethiopian rift: birth of a triple junction, *Earth planet. Sci. Lett.*, **224**(1), 213–228.

SUPPORTING INFORMATION

Additional Supporting Information may be found in the online version of this paper:

Figure S1. Correlation map of magnetic anomaly profiles, projected along N35°E (northern and central Red Sea) or N°25E (southern Red Sea), according to the general trend of fracture zones. Black lines are observed data, brown lines are theoretical profiles, calculated along existing data profiles with fixed spreading rate. Dashed line represents the ridge axis, correlation isochrons C2n.1n(y), C2An.1n(y) and C3n.1n(y) are represented by green, ocra and purple lines, respectively.
Figure S2. Magnetic anomaly identification of profile 83010001.2.
Figure S3. Magnetic anomaly identification of profile 83010001.3.
Figure S4. Magnetic anomaly identification of profile 83010001.6.
Figure S5. Magnetic anomaly identification of profile 83010001.7.
Figure S6. Magnetic anomaly identification of profile 83010001.8.
Figure S7. Magnetic anomaly identification of profile 83010001.9.
Figure S8. Magnetic anomaly identification of profile 83010001.10.
Figure S9. Magnetic anomaly identification of profile 83010001.11.

Figure S10. Magnetic anomaly identification of profile 83010001.12.
Figure S11. Magnetic anomaly identification of profile 83010001.13.
Figure S12. Magnetic anomaly identification of profile 83010001.14.
Figure S13. Magnetic anomaly identification of profile 83010001.15.
Figure S14. Magnetic anomaly identification of profile 83010001.16.
Figure S15. Magnetic anomaly identification of profile 83010001.17.
Figure S16. Magnetic anomaly identification of profile 83010001.18.
Figure S17. Magnetic anomaly identification of profile 83010001.19.
Figure S18. Magnetic anomaly identification of profile 83010001.20.
Figure S19. Magnetic anomaly identification of profile 83010001.21.
Figure S20. Magnetic anomaly identification of profile 01010029.3.
Figure S21. Magnetic anomaly identification of profile 83010001.23.
Figure S22. Magnetic anomaly identification of profile 02010051.2.
Figure S23. Magnetic anomaly identification of profile 83010001.24.
Figure S24. Magnetic anomaly identification of profile 83010001.25.
Figure S25. Magnetic anomaly identification of profile 83010001.26.
Figure S26. Magnetic anomaly identification of profile 83010001.27.
Figure S27. Magnetic anomaly identification of profile 83010001.28.
Figure S28. Magnetic anomaly identification of profile 02010051.3.
Figure S29. Magnetic anomaly identification of profile 83010001.30.
Figure S30. Magnetic anomaly identification of profile 83010001.31.
Figure S31. Magnetic anomaly identification of profile 83010001.32.
Figure S32. Magnetic anomaly identification of profile 83010001.33.
Figure S33. Magnetic anomaly identification of profile 83010001.34.
Figure S34. Magnetic anomaly identification of profile 83010001.35.
Figure S35. Magnetic anomaly identification of profile 83010001.38.
Figure S36. Magnetic anomaly identification of profile 83010001.39.
Figure S37. Magnetic anomaly identification of profile 83010001.40.
Figure S38. Magnetic anomaly identification of profile 83010001.41.
Figure S39. Magnetic anomaly identification of profile 83010001.42.
Figure S40. Magnetic anomaly identification of profile 83010001.43.
Figure S41. Magnetic anomaly identification of profile 02010051.5.
Figure S42. Magnetic anomaly identification of profile 83010001.44.
Figure S43. Magnetic anomaly identification of profile 01030352.3.
Figure S44. Magnetic anomaly identification of profile 02010051.6.
Figure S45. Magnetic anomaly identification of profile 01030352.2.
Figure S46. Magnetic anomaly identification of profile 02010051.7.
Figure S47. Magnetic anomaly identification of profile 01010029.2.
Figure S48. Magnetic anomaly identification of profile 02010051.8.
Figure S49. Magnetic anomaly identification of profile 02010027.2.
Figure S50. Magnetic anomaly identification of profile 19050009.2.
Figure S51. Magnetic anomaly identification of profile 02010027.3.
Figure S52. Magnetic anomaly identification of profile 19050009.3.
Figure S53. Magnetic anomaly identification of profile 19050009.4.
Figure S54. Magnetic anomaly identification of profile 19050009.5.
Figure S55. Magnetic anomaly identification of profile 01010029.1.
Figure S56. Magnetic anomaly identification of profile 02010051.10.
Figure S57. Magnetic anomaly identification of profile 01030352.7.
Figure S58. Magnetic anomaly identification of profile 19050009.6.
Figure S59. Magnetic anomaly identification of profile 19050009.7.
Figure S60. Magnetic anomaly identification of profile 19050009.8.
Figure S61. Magnetic anomaly identification of profile 19050009.9.
Figure S62. Magnetic anomaly identification of profile 19050009.10.
Figure S63. Magnetic anomaly identification of profile 19050009.11.
Figure S64. Magnetic anomaly identification of profile 19050009.12.
Figure S65. Magnetic anomaly identification of profile 19050009.14.
Figure S66. Magnetic anomaly identification of profile 19050009.15.
Figure S67. Magnetic anomaly identification of profile 19050009.18.
Figure S68. Magnetic anomaly identification of profile 19050009.19.
Table S1. Focal mechanism used in the determination of the seismic strain rates in the Afar region.
Table S2. Focal mechanism used in the determination of the seismic strain rates in the Sinai region (http://gji.oxfordjournals.org/lookup/suppl/doi:10.1093/gji/ggw280/-/DC1).